# The 3D submicron-scale skeletal reconstruction of *Nannoconus* (Cretaceous calcareous nannofossil) - Insights ~~on~~ **into** biomineralization

Rajkumar Chowdhury[1,2,3], Redhouane Boudjehem[4], Baptiste Suchéras-Marx[5], Maxime Dupraz[4], Anico Kulow[4], Julio Cesar da Silva[4], Jean Louis Hazemann[4], Marie-Pierre Aubry[6], Javier Pérez[7], Alejandro Fernandez-Martinez[1], Fabienne Giraud[1]

[1]Univ. Grenoble Alpes, Univ. Savoie Mont Blanc, CNRS, IRD, Univ. Gustave Eiffel, ISTerre, 38000 Grenoble, France
[2]LGL-TPE - (UCB, Lyon1 - UJF - UMR CNRS 5276 - ENS de Lyon - 46, Allée d'Italie - 69364 Lyon cedex 07 - France)
[3]Pôle d'Etudes et de Recherche de Lacq, TotalEnergies, BP 47 - RD 817, 64170, Lacq, France
[4]Univ. Grenoble Alpes, CNRS, Institut Néel, 38042 Grenoble, France
[5]Aix Marseille Univ, CNRS, IRD, INRAE, CEREGE, Aix-en-Provence, France
[6]Department of Earth and Planetary Sciences, Rutgers University, New Brunswick, New Jersey 08854, USA
[7]SWING Beamline, Synchrotron SOLEIL, L'Orme des Merisiers, Départementale 128, 91190 Saint-Aubin, France

*Correspondence to*: Rajkumar Chowdhury (rajkumar.chowdhury@ens-lyon.fr)

**Abstract.** *Nannoconu*s (~5-20 μm) was a major planktonic producer in the Early Cretaceous seas (~150-120 Ma). The heavy calcitic skeletons (~200-1400 picogram) of this calcareous nannofossil have contributed to massive carbonate accumulations for over ~30 million years. The skeletal microstructure is characterized by an interlocking arrangement of calcitic lamellae spanned around a central canal. The biomineralization process involved in producing the sophisticated skeleton is investigated for the first time. Ptychography X-ray computed tomography (PXCT) with synchrotron radiation is applied to an isolated skeleton, to obtain a 3D set of tomographic images with ~ 40 nm spatial resolution. This 3D set was processed to virtually segment the individual calcitic lamella and reconstruct the full skeleton through constraining different lengths and angles. The lamellae are repetitively stacked in two distinct inclinations, one following the other, and producing segments combined to form the entire skeleton. Individual lamellae were calcified in a "template" of organic layer containing amino acid(s)/biomolecule(s), responsible for creating the interlocking arrangement. Our study of *Nannoconus* provides a simple yet potent approach to the analysis of biomineralized microstructures characterized by the repetitive arrangement of calcitic units as commonly seen in the calcareous nannoplankton.

# 1 Introduction

Calcareous nannofossils (~1-30 μm) are biomineralized calcitic remains of marine planktonic unicellular algae (Siesser and Winter 1994) and are abundant in the sedimentary archives. Initially rare, calcareous nannofossils became increasingly abundant in marine sediments to reach an optimum in the Cretaceous, around ~120 Ma (Suchéras-Marx et al., 2019) and they profoundly altered the dynamics of the carbonate and oceanic carbon cycle (Erba, 2006). Among calcareous nannofossils, *Nannoconus* was the major biocarbonate producer in the Early Cretaceous seas (~152-120 Ma) (Bown, 2005) with the largest size (~5-20 μm) and the heaviest mass (~200-1400 picogram) of the calcitic skeleton, contributing to massive carbonate accumulations over ~30 million years. These massively produced biocalcites most likely had significantly modified the marine chemistry significantly, upon transfer to the oceanic sedimentary record, with possible consequences on the marine biosphere at a time of important planktonic diversification (Hart et al., 2003; Kooistra et al., 2007). Despite the importance of this group, knowledge of the organism that produced the calcitic skeleton of *Nannoconus* is non-existent. A proper understanding of the biomineralization process from the 3D microstructural arrangement of the skeleton, obtained from a finely-resolved physical characterization, can help to close this gap.

With advances in imaging techniques, several high-resolution characterization methods have been successfully applied to biocalcite produced by extant planktonic algae or preserved as fossils. These techniques include AFM (Henriksen et al., 2004), 3D-FIB-SEM (Hoffmann et al., 2015) and cryo-electron tomography (Walker et al., 2020). In addition, several X-ray scattering methods with synchrotron radiation also have been applied, such as 2D (Suchéras-Marx et al., 2016a) and 3D (Walker et al., 2024) X-ray microfluorescence, X-ray Coherent Diffraction (Beuvier et al., 2019). Ptychographic X-ray computed tomography (PXCT) (Dierolf et al., 2010) is a non-destructive tomographic reconstruction imaging method that can be applied to characterize fossilized biocalcite. In this study, we performed the a Ptychography X-ray computed tomography (PXCT) experiment using synchrotron radiation at the SWING Beamline of the SOLEIL (French synchrotron). Our primary focus was on the well-preserved on well preserved skeletons of *Nannoconus* to investigate its microstructural arrangement at the nano-scale resolution. The experiments generated tomographic volumes of the samples with a 3D spatial resolution of approximately 30 nm. Subsequently, we analyzed these volumes using image visualization software and successfully reconstructed the complete 3D skeleton of a single *Nannoconus* specimen, specifically, *N. globulus* for the first time. This strategy serves as a methodological framework for reconstructing the *Nannoconus*'s skeletal structure in general. Subsequently we analyzed these volumes using image visualization software and successfully reconstructed the complete 3D skeleton of *Nannoconus* for the first time. As direct biological evidence is absent for this extinct group of calcareous nannoplankton producing such massive skeletons, i.e., *Nannoconus*, Thethe The knowledge of the structural constraint of the 3D skeletal arrangement obtained from the aforementioned reconstruction has been used to provide perspectives on *Nannoconus* its biomineralization process. The knowledge of the 3D microstructural arrangement obtained from the aforementioned reconstruction has been used to provide

~~perspectives on the biomineralization process of the extinct group of calcareous nannoplankton producing such massive~~
60 ~~skeletons i.e., *Nannoconus*.~~


## 2 The *Nannoconus* skeleton

*Nannoconus* is a Genus (Kamptner, 1931, emend. Farinacci, 1964) belonging to the Family of *Nannoconaceae* (Reinhardt, 1966) (Table C1 in the Appendix). This Family is included in the Order of *Braarudosphaerales* (Aubry, 2013, Aubry, 2025) by Lees and Bown (2016). ~~This Order was originally introduced for Cenozoic (~66 Ma to present) coccoliths, another group~~
65 ~~of calcareous nannofossils.~~ *Nannoconus* is mostly a genus of Tethys domain which spans from the latest Jurassic (Tithonian, ~145 Ma) through the late Cretaceous (Campanian, ~72 Ma) (Perch Nielsen, 1985). However, in the Tethys domain, it is only abundant until the end of the Aptian (~113 Ma), which is the end of the climax of *Nannoconus* (Erba, 1994). This represents a duration of ~30 Myr, during which the skeleton exhibits a great morphological diversity (Derès and Achéritéguy, 1980).


70 **2.1 Morphology**

Different species have been described for the Genus *Nannoconus* and are characterized by different shapes of the skeleton. These include cylindrical, globular, hour-glass, and conical (Figs. 1a-1d). Van Niel (1993) introduced several terms to describe it. Some of these terms are used in this study (Figs. 1e and 1f). The *wall* encloses the *central canal* which runs along the longitudinal axis of the skeleton with two terminal openings known as *apertures*. Several morphogroups of *Nannoconus* have
75 been defined based on the general shape and size of the skeleton (Brönnimann, 1955; Bouché, 1965; Derès and Achéritéguy, 1972; Aubry, 1974), the shape of the central canal (Brönnimann, 1955; Bouché, 1965), the thickness and construction of the wall (Brönnimann, 1955; Bouché, 1965; Derès and Achéritéguy, 1972; Aubry, 1974), the shape and the size of the terminal openings (Brönnimann, 1955; Bouché, 1965; Derès and Achéritéguy, 1972; Aubry, 1974).
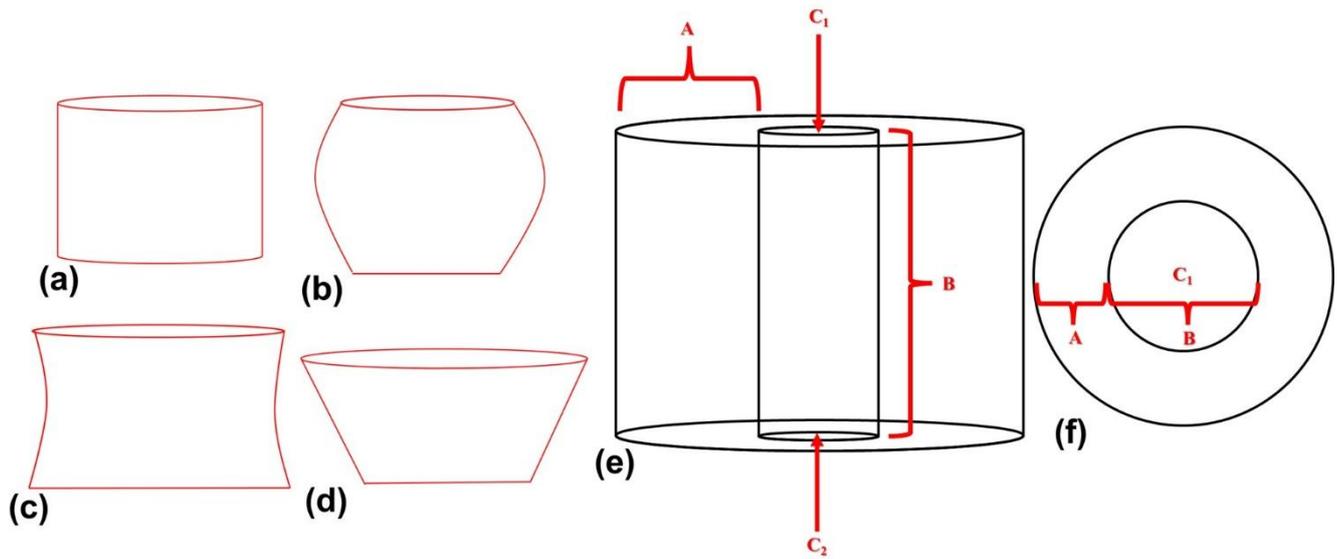
**Figure 1:** <mark>Schematic diagrams illustrating four different skeletal morphologies of four different species of *Nannoconus*. These are (a) cylindrical, (b) globular, (c) hour-glass, and (d) conical as observed in *Nannoconus truittii*, *Nannoconus globulus*, *Nannoconus abundans*, and *Nannoconus steinmannii* respectively.</mark> **(e and f) Longitudinal and transverse views, respectively, of the schematic illustration of a cylindrical skeleton. In this figure, A and B represent the wall and the central canal respectively. $C_1$ and $C_2$ are the two terminal apertures. It should be noted that the shape of the central canal differs with the general morphology of the skeleton.**

## 2.2 Microstructure

The wall of *Nannoconus* consists of interlocking sub-rhombohedral (Van Niel, 1994) to semi-circular plates (Stradner and Grun, 1973) (length ~0.5-1 µm, thickness ~0.1-0.5 µm) (Kamptner, 1931; Trejo, 1960; Derès and Achéritéguy, 1972; Van Niel, 1993, 1994). Two distinct types of plates (green and yellow lines in Fig. 2a) build the skeleton. Each plate is characterized by a specific inclination, measured from a horizontal line (blue line in Fig. 2b). These nannofossils have been defined by Aubry (2013) as <mark>"homococcoliths,</mark> i.e., coccoliths consisting of identical, imbricated segments that are stacks of lamellae of similar shape". <mark>Here, the term "lamellae" refers to the plates of Van Niel (1993) and this term is retained in this work. The term "homococcolith" has been replaced as "micalith" by Aubry (2025).</mark>

Based on 2D scanning electron microscopy (SEM) studies, some authors (Aubry, 1974, 2013, 2025; Van Niel, 1993) attempted to explain the 3D microstructural arrangement. Currently, two different concepts of skeletal construction are proposed. The first concept is based on a layering of two types of plates (Van Niel, 1993; Lees and Bown, 2016), the second concept is based on an organization of lamellae in segments (Aubry, 2013, 2025) of *Nannoconus*. They can be summarized as the following two models:
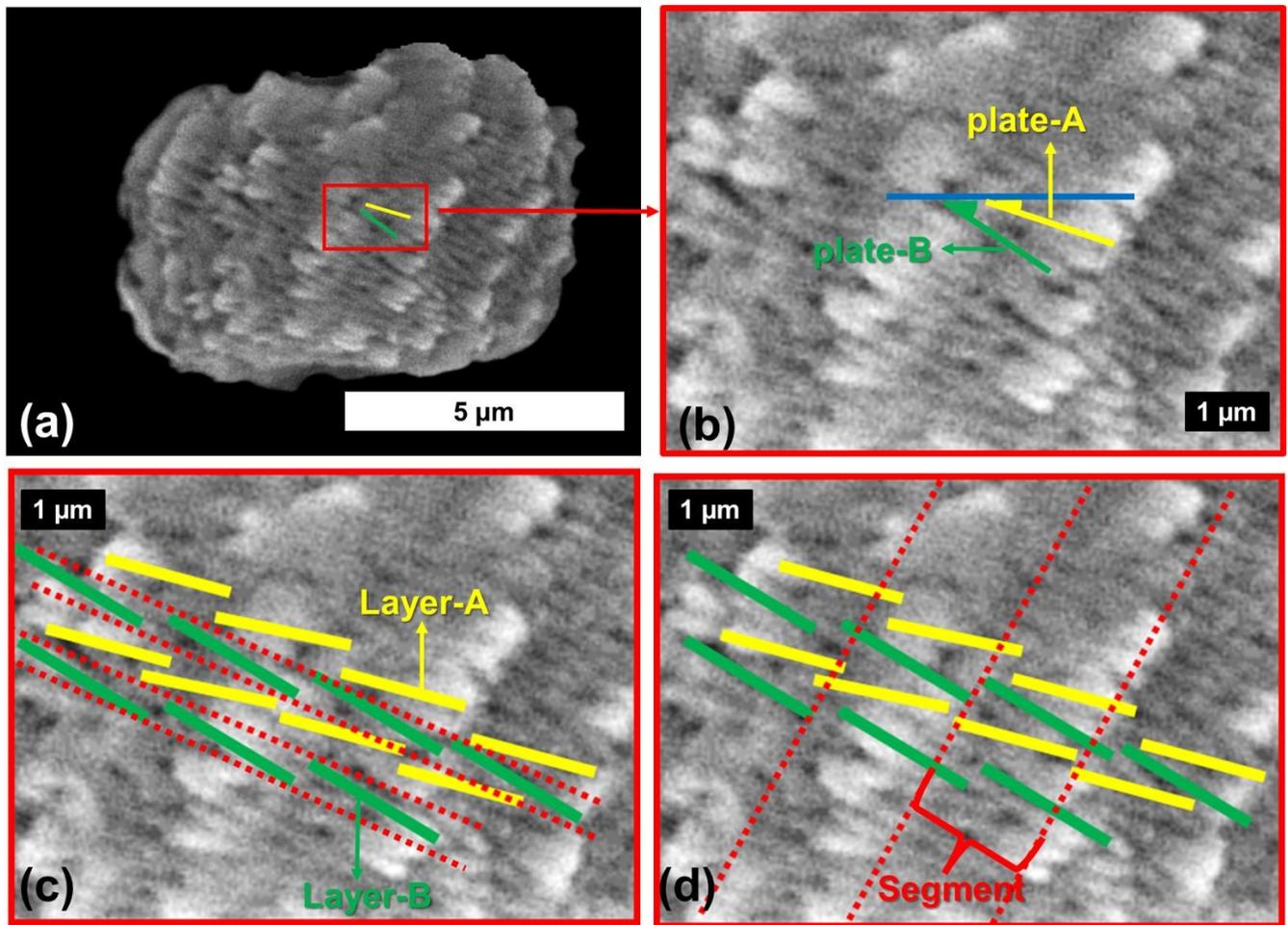
**Figure 2: Scanning electron microscopic (SEM) image of *Nannoconus globulus*. (a) Longitudinal view. The solid green and yellow lines inside the red box highlight the two distinct types of plate-A and -B. (b) Closer view of the plate-A and plate-B shown in (a), with the inclinations measured from the blue horizontal line. (c) Arrangement of plates -A and -B in two layers (-A is yellow and -B is green). The red-dotted line separates the two consecutive layers. (d) Oblique arrangement of the segments composed of alternating plate-A (yellow) and -B (green). Consecutive segments are individualized by red dotted lines. "Plates" are used following the terminology of Stradner and Grun (1973) and Van Niel (1993); they have been referred to as "lamellae" by Aubry (2013). The term "lamellae" is retained throughout this work.**

### 2.2.1 Model-1

In Van Niel (1993), the plates with a lower angle of inclination (yellow) are termed plate-A and the plates with a higher angle of inclination (green) are termed plate-B. Plate-A and -B form two distinct types of layers (Fig. 2c) named as layer-A and layer-B respectively. The skeleton can be understood as a combination of these two types of spiral layers of plates alternatively arranged one after another. This can be explained in Fig. 2c: first, a layer-B (green lines) is placed, followed by a layer-A (yellow lines). Over layer-A, another layer-B is again placed. Delimitation of layers is marked by red dotted lines (Fig. 2c).

5

Van Niel (1993) distinguished nine different morphogroups (Table C1 in the Appendix) of *Nannoconus*, based on the various inclination(s) of plate-B and the width(s) between two consecutive layers of plate-A.

In a SEM image of the species *Nannoconus globulus* (Brönnimann, 1955) (selected for the present study), it is possible to
115    count six plates with two distinct angles of inclination in the part where the plates are well-preserved (Figs. B1a and B1b in the Appendix). This part constitutes about half of the circular aperture (180°). Thus, the total number of plates in the full circular aperture (360°) would be =12, with six plate-A and six plate-B. Considering that each of these plates belongs to a separate layer, there are six layer-A and six layer-B, i.e., a total of 12 layers in the whole skeleton.

### 2.2.2 Model-2

120    As suggested by Aubry (2013, 2025), the skeleton is a combination of identical, imbricated segments. These segments are formed by stacking lamellae (Fig. 2d) of similar shape (Fig. 12d in Aubry, 2025). Lamella-B (green line) and lamella-A (yellow line) are organized two by two to form duos. Duos of lamellae are stacked to compose a segment. Therefore, the spiral combination of several such segments forms the entire skeleton. Three such segments are delineated by red dotted lines in Fig. 2d.

125    In a SEM image (Fig. B1c in the Appendix) of *N. globulus* described above (in model-1), six segments in the part where the skeleton is well-preserved, can be detected. As this part constitutes about 1/2 of the circular aperture (180°), the total number of segments in the full circular aperture would be 6*2 = 12. Therefore, the total number of the segments in the full skeleton of *Nannoconus* = 12.

It should be noted that these two concepts only explain the skeletal microstructure and do not provide any information about
130    the parameter(s) controlling the shape of the skeleton. To address the validity of the two models and also to decipher the parameter(s) influencing the skeletal shape and microstructure from the 3D skeletal reconstruction, a synchrotron-based PXCT was conducted.

### 2.3 Stratigraphy

*Nannoconus* spans from the latest Jurassic (Tithonian, ~145 Ma) through the late Cretaceous (Campanian, ~72 Ma) (Perch-
135    Nielsen, 1985). However, it is only abundant until the end of the Aptian (~113 Ma) which is the end of the climax of *Nannoconus* (Erba, 1994). This represents a duration of ~30 Myr, during which the skeleton exhibits a great morphological diversity (Derès and Achéritéguy, 1980).

## 3 Materials and Methods

### 3.1 Material

140  Six specimens representing five different species of *Nannoconus* have been used for the Ptychographic X-ray Computed Tomography (PXCT) experiment. They come from the Aptian (Covington and Wise, 1987) calcareous sediments of the DSDP Leg-93-Site 603 (continental rise of the western margin of the North Atlantic) core 44, interval 115-116 cm. They have been selected for their good state of preservation as determined through scanning electron microscopy (SEM images of *Nannoconus* are shown in Fig. B2 in the Appendix). Here, "good state of preservation" refers to skeletons which are structurally fully intact

145  without any breakage and devoid of post-depositional growth of calcite, that often obscures the microstructure of nannofossils. We focus our study on the species *N. globulus* to illustrate the microstructural arrangement and the 3D reconstruction of the skeleton. This globular skeleton exhibits a well-defined interlocking pattern of the lamellae.

### 3.2 Sample Preparation

The PXCT experiment required the picking of an individual single specimen of *N. globulus* with a silica needle (Figs. B3a and
150  B3b in the Appendix) (modified from Suchéras-Marx et al., 2016b). The needle was then placed in a metal holder (Fig. B3c in the Appendix), directly placed at the experimental station of the beamline.

### 3.3 Ptychography computed X-ray tomography (PXCT)

Ptychography is an advanced X-ray imaging technique that involves capturing a series of far-field diffraction patterns from overlapping areas of a sample. These diffraction patterns are then used in a computational phase retrieval algorithm to
155  reconstruct a high-resolution two-dimensional image. In the field of PXCT, ptychography is combined with tomography. This process involves performing ptychographic experiments at different tomography angles, which produces highly spatially resolved, detailed tomographic projections. As a result, PXCT offers a thorough three-dimensional (3D) representation of the microstructure of the sample, achieving nanometric resolution. This enhances the ability to analyse complex materials at a microstructural level. After obtaining the 3D images, it is essential to examine the resulting high-resolution tomographic
160  volume of biocalcite using advanced 3D image analysis techniques. Methods such as image segmentation and visualization (Reznikov et al., 2020) are necessary to extract relevant microstructural properties from the sample.

The experiments were performed at the SWING beamline at SOLEIL-Synchrotron, Paris, France. The photon energy was of 8.00 keV, and the sample-to-detector position was set to 6.484 m. The ptychography experiments were carried out with a beam size of about 4 µm at the sample position and a scanning step size of 1.0 µm. A number of 164 positions were collected and
165  distributed as concentric circles within a rectangular field of view of 20 µm x 10 µm (HxV). We used a region of interest of 1000 x 1000 pixels of an EIGER-4M in-vacuum detector from DECTRIS with a pixel size of 75 µm. For the PXCT experiments (Dierolf et al., 2010), 632 tomographic projections were acquired between 0° and 180°, with exposure time of 100 ms, as 8 interlaced sub-tomograms. The resulting diffraction patterns were transformed into real space projections using the Ptycho-

Shelves (Wakonig et al., 2020) suite from the cSAXS team at Paul Scherrer Institute, with a starting probe model previously determined experimentally using a Siemens Star ptychographic scan. The final volume was determined from the tomographic projections using the Matlab tomography package within PtychoShelves.

## 4 Results

### 4.1 Descriptive parameters

The combination of the tomographic image slices, obtained from PXCT, reveals the external and internal views of the *N. globulus* skeleton. These observations of this *Nannoconus* are presented here to understand the shape of the skeleton and the arrangement of lamellae and to propose a set of standard parameters that can be used to describe other *Nannoconus* morphogroups.

In the following, cylindrical coordinates are used to describe the skeletal microstructure in terms of the positions and orientations of the constituting lamellae (Figs. 3a-3d). The $z$-axis is parallel to the longitudinal view of the skeleton, passing through the central canal. The Radius, $r$, corresponds to a vector going from the center of mass of the single lamella to the center of the central canal, and it is perpendicular to the $z$-axis. For the purpose of this geometric description, the lowest and the highest points of the skeleton in longitudinal orientation are defined as base and apex, respectively (Fig. 3a). The total vertical length between the base and apex is given by L (Fig. 3a). The length of the radius (r) is measured from the central axis to the end of the wall (Fig. 3a). It changes throughout the whole skeleton from the base to the apex. Starting from the base, the radius increases, reaching a maximum and decreasing towards the apex, giving the skeleton a globular shape. This also indicates that the radius value is maximum at $2/3^{rd}$ of the length (measured longitudinally) between the base and the apex. The minimum value of the radius is observed at the base of the skeleton (Fig. 3a). Two angles define the spatial orientation of each lamella. The first angle was previously defined by Van Niel (1993), based on the SEM images and is Inclination ($\delta$). In the cylindrical coordinates described before, it corresponds to the angle (Fig. 3b) formed between the lamella and an axis corresponding to the radius (blue line in Fig. 3b). Two sets of lamellae with different inclinations are shown in Fig. 3c: the lamella with low inclination ($\delta_A$, yellow line given by VW), is named lamella-A. The lamella with high inclination ($\delta_B$, green line given by XY), is termed as lamella-B (Fig. 3c). Lamella-A + lamella-B formed twin lamellae. The term "twin lamellae" describes the repeating pair of lamellae (i.e., lamella-A and lamella-B), with alternating inclinations that together construct the full skeleton of *Nannoconus*. The second angle (Fig. 3d), called Tilt ($\tau$), corresponds to the angle formed between a lamella and an axis of rotation perpendicular to the radius (red line in Fig. 3d). Tilt values are of opposite sign for lamellae placed in the upper (high z) or lower (low z) parts of the skeleton (Fig. 3d). As mentioned above, the arrangement of the lamellae has been described in two models in the literature. Here, we will show that the components (the layers in model-1 and the segments in model-2) of the two models can be verified using the abovementioned radius and angles.

8
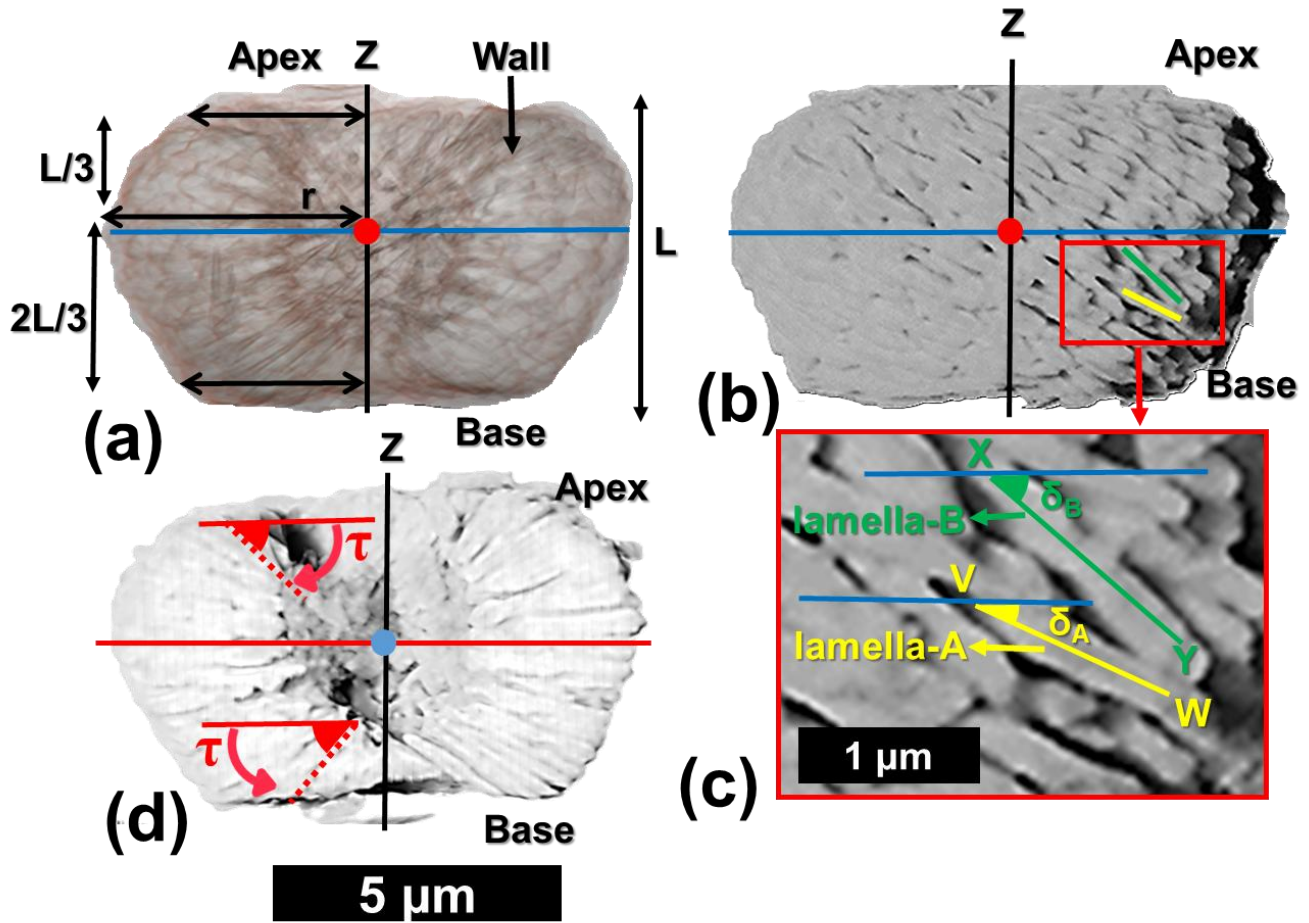
**Figure 3: Description of the parameters for the reconstruction of the 3D skeletal microstructure of *N. globulus* using the results of the PXCT experiment. (a) Internal view of *N. globulus*. The microstructure is interpreted using a cylindrical coordinate system. The red dot indicates the radial axis (perpendicular to the plane of the paper), and the blue line represents an axis perpendicular to the radius. The z-axis, marked by the black line, passes longitudinally through the central canal. The length of the red arrows corresponds to the radius, measured from the z-axis to the end of the wall of the skeleton. The radius increases initially from the base for 2/3$^{rd}$ of the length (L) of the *Nannoconus*, and then decreases towards the apex for the remaining 1/3$^{rd}$ of the length (L). (b) External view of the same specimen of *N. globulus*, in the cylindrical coordinate system. (c) Magnified skeletal microstructure of the part delineated by the red box in (b), illustrating the two lamellae types: lamella-A (yellow) and lamella-B (green). Their inclinations, $\delta_A$ and $\delta_B$ respectively, correspond to the angles measured between the blue line (axis perpendicular to the radius) and each lamella. (d) Cross-section of *N. globulus* across the length. The angle measured between the lamella and the red line (radial axis) defines the tilt. The tilts of the lamellae at the base (lower z) are opposite in direction with respect to the lamellae at the apex (upper z).**

### 4.2 Segmentation of a lamella

The first step in our analysis of the PXCT data was to isolate one lamella (Figs. 4a-4g). The experiment resulted in a series of tomographic image slices for the whole skeleton. These images reveal overlapping lamellae within the interior of the skeleton, likely resulting from diagenetic alteration (a process involving the dissolution of the biocalcite, produced during the biomineralization and subsequent reprecipitation). Although the specimen was considered "well-preserved" based on SEM

9

imageselectron microscopy, the result of higher spatial resolution of the PXCT revealpresents clear diagenetic effects within the *Nannoconus*'s skeleton. As a consequence, individual lamellae are sometimes difficult to segment (i.e., virtually separate) in the tomographic images. Also, despite having a spatial resolution of ~30–40 nm, this resolution is at the same scale of the thickness of the lamellae themselves and is therefore insufficient for distinctly segmenting a single lamella. Despite having a satisfactory spatial resolution of ~30-40 nm, the lamellae are sometimes difficult to segment (i.e., virtually separate) from the images. This is caused by internal overlapping of the lamellae and by the limited spatial resolution at the same scale of the lamella thickness. To overcome this problem, all the images were filtered using Contrast Limited Adaptive Histogram Equalization (CLAHE) (Reza, 2004). This increased the contrast of the images and hence helped to delineatesee more clearly the boundaries between the lamellae more clearly. After this contrast enhancement, a single lamella was segmented by selecting by hand regions of interest for each slice. Four such slices are shown in Figs. 4a-4d. This results in a 3D volume of the lamella that was exported and used to reconstruct the structure of the skeleton using our models (Figs. 4e and 4f). Given the high amount of data, the convex hull (Table C1 in the Appendix; Ky, 1959) of the 3D volume of the segmented lamella (Fig. 4g) was generated using Python routines and utilized for the reconstruction of the models. However, this manual segmentation approach is not applicable to the entire *Nannoconus* because: (A) It is extremely time consuming to manually segment numerous lamellae of *Nannoconus*, from ~300 tomographic image slices. (B) The lamellae frequently overlap with each other, due to post-depositional overgrowth (a process that dissolves and reprecipitates the calcite), making them difficult to distinguish for segmentation. Hence, we have segmented a distinctly identifiable lamella and utilized it as a unit to reconstruct the entire skeleton. As described earlier, *Nannoconus* belongs to *Braarudosphaerale* Order (Aubry, 2013, 2025), which is defined (Aubry, 2013) as "consisting of identical, imbricated segments that are stacks of lamellae of similar shape". Therefore, it can be inferred that *Nannoconus*'s lamellae are also of "similar" shape/morphology. To check this, we have segmented another lamella (Fig. 4h) from a different part of the skeleton (different from Fig. 4e), whose convex hull of this lamella is given in Figure 4i. The segmented lamellae are of triangular, flat shape, ~2.00 μm long and ~0.50 μm thick. Both of the lamellae present a similar shape/morphology (Figs. 4g and 4i). Based on the morphological similarity between two lamellae from different parts of the skeleton, we concluded that the entire skeleton of *N. globulus* is composed of morphologically similar lamellae.
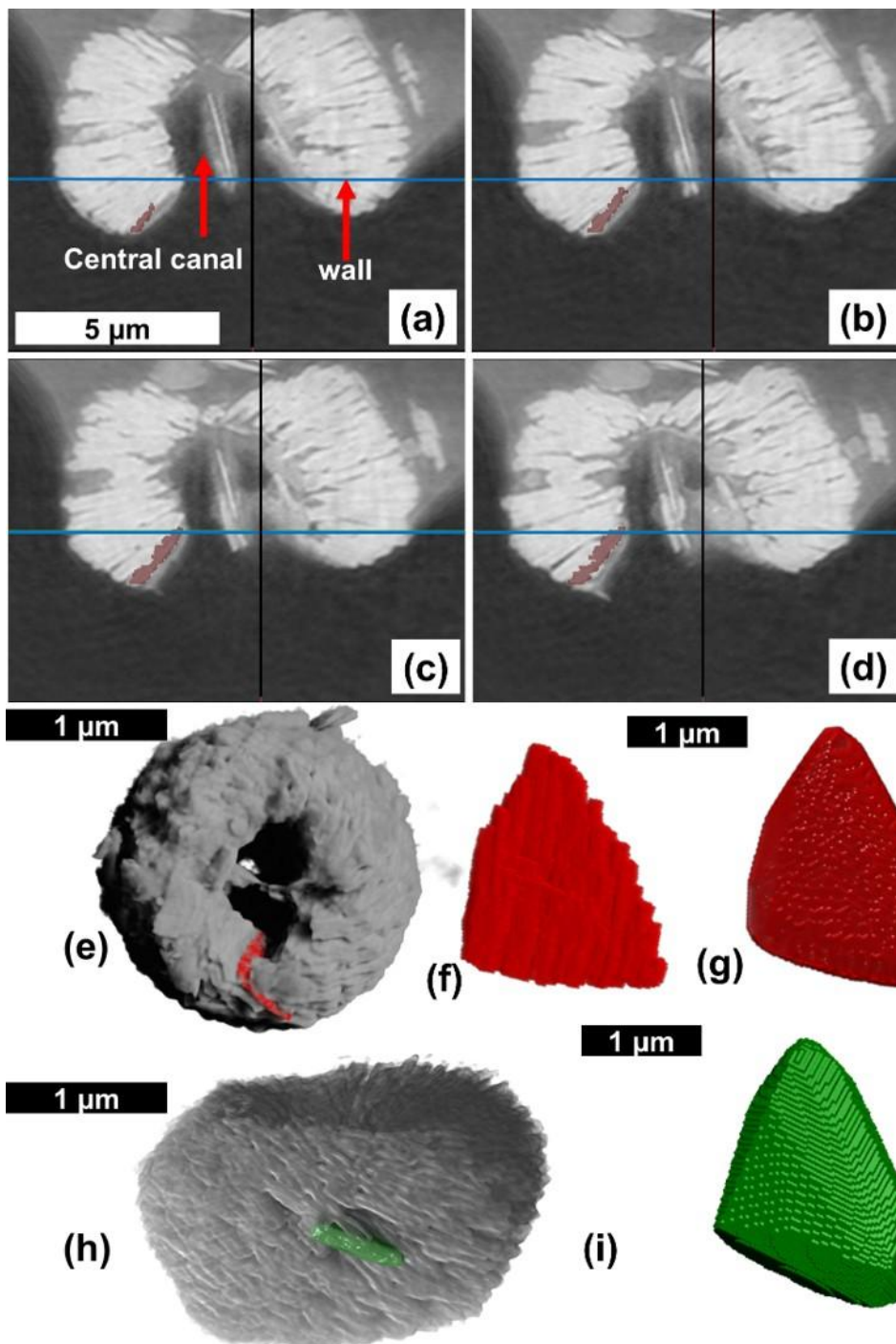
Figure 4: Procedures describing the segmentation/virtual separation of a lamella from the result of the PXCT analysis of *N. globulus*. (a-d) Four consecutive tomographic images obtained from the PXCT analysis of *N. globulus* with the wall and central canal. The part present within the central canal is possibly a lamella detached from the wall. (e) The marked lamella (red colour) is presented within the skeleton. (f) Isolated individual lamella after the segmentation. (g) Convex hull of the lamella, with smooth edges and surfaces. Convex hull (See Table C1 in the appendix) is the mathematical representation of an envelope covering the segmented

11

lamella. **(h) Another segmented lamella (green colour) is marked within the skeleton. (i) Convex hull of the segmented lamella, marked in (h).**

## 4.3 Reconstruction

250 We developed a code using Python script (Van Rossum and Drake, 2009) directly in a console attached to the image visualization software to reconstruct the skeleton using the segmented lamella. The process of the skeletal reconstruction from the segmented lamella can be described as:

### 4.3.1 Generation of inclination and tilt

The lamella (given by ABC in Fig. 5a), which has a triangular, flat shape, is rotated in two perpendicular directions in a
255 cylindrical coordinate system to set values for inclination and tilt. The procedure is as follows:

1. The rotation with the radial axis as the axis of rotation generates the inclination, $\delta$, of the lamella (Figs. 5b and 5d).

2. The rotation with the axis perpendicular to the radial axis (Figs. 5c and 5d) as the axis of rotation generates the tilt, $\tau$, of the lamella.
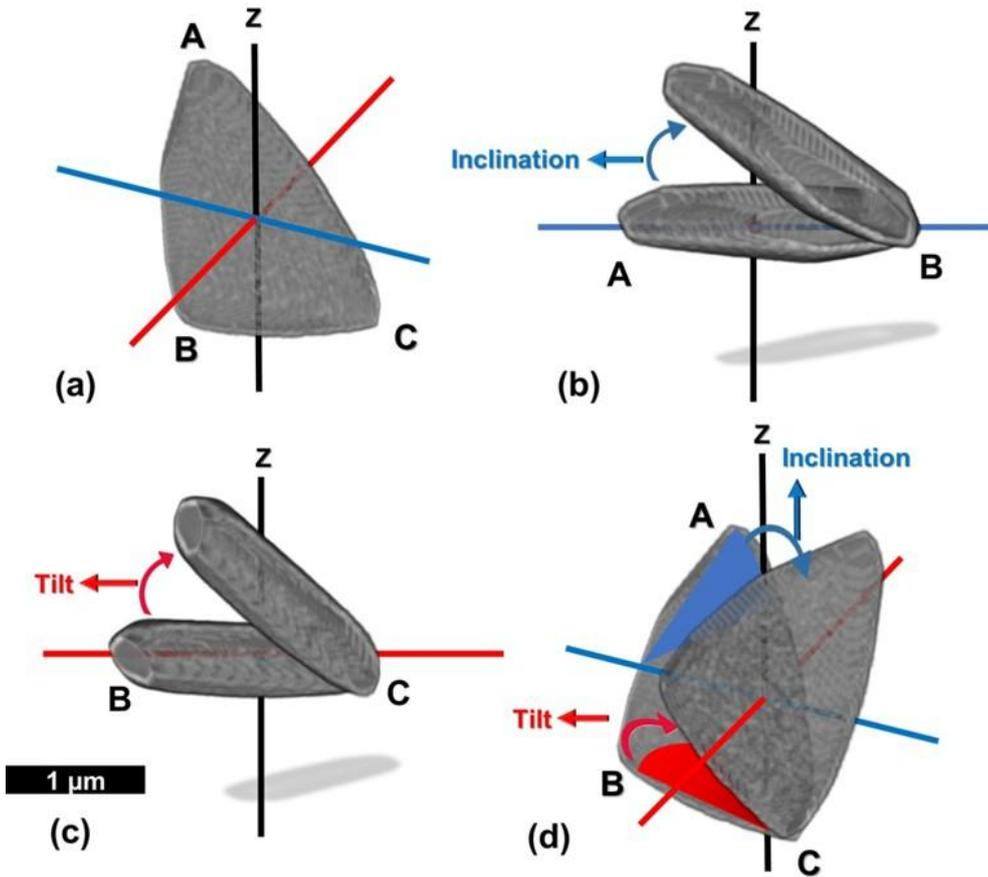
Figure 5: Generation of the inclination and tilt in the segmented lamella. (a) The segmented lamella, given by ABC, is placed in the cylindrical coordinate system with one vertical z-axis (black line) and two radial axes (red and blue lines). (b) The rotation of the lamella, where the radius (red line) is the axis of rotation, creates inclination, and the rotation angle is measured between the lamella and the blue line. (c) The rotation of the lamella, where the axis perpendicular to the radius (blue line) is the axis of rotation, creates tilt, and the rotation angle is measured between the lamella and the red line. It should be noted that the axes of rotation for creating inclination and tilt are perpendicular to the lines from which the individual angle of inclination and tilt are measured. (d) The combination of two perpendicular rotations in the cylindrical coordinate, creates the inclination and tilt in the segmented lamella.

### 4.3.2 Formation of points in spiral axes

The skeleton being conceptualized as a combination of spiral layers/segments, it is now necessary to create the layers/segments utilizing the segmented lamellae. A series of points forming spiral axes was generated to place individual lamellae, creating layers/segments. The points of a series are defined following cylindrical coordinates (Fig. 6a):

i) The radius, r, given by the distance from the central axis to the center of mass of the lamella.

ii) The azimuth, ɵ, given by the angle around the central axis.

13
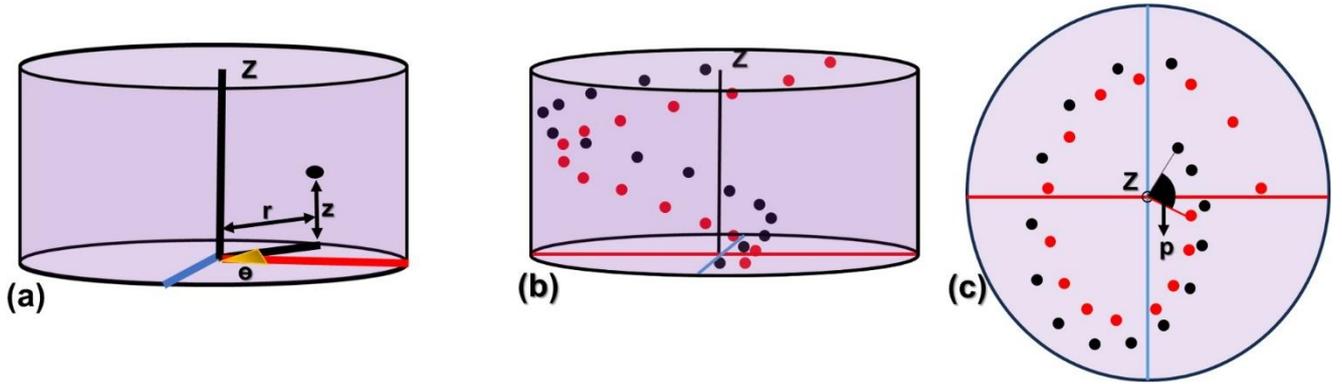
Figure 6: Presentation of the series of points in spiral axes to form the layers and segments in the cylindrical coordinate system. (a) Radius (r), azimuth (ϴ), and vertical distance (z) that define a point in the cylindrical coordinate system. The red line represents the radial axis, and the blue line represents a line perpendicular to it. (b, c) Longitudinal and transverse views, respectively, of the two series of points defined by the black and red dots in the cylindrical coordinate system, representing two consecutive layers/segments. Here, "p" marks the angular separation between the two series of points.

Values of r, ϴ, and z are generated so that the lamellae fully occupy the space, forming a compact skeleton in visual accordance with the 3D reconstruction obtained from the PXCT data. Here, the first and last points represent the base and the apex of the skeleton, respectively. Considering the total number of points in the series is n, an $i^{th}$ point ($r_i$, $\theta_i$, $z_i$), [where i<n] in the series is represented by the following equations:

$ri = R + i * rstep$ [if i<=2*n/3] (radius increases for the first 2*n/3 points) and $ri = r(i-1) - i * rstep$ [if i>2*n/3] (radius decreases the last n/3 points) (1). This results in a globular shape for the skeleton.

R = Initial radius, $r_{step}$ = (Maximum radius-Minimum radius)/n.

$\theta i = (\theta + i * \theta step)$ (2)

ϴ = Initial azimuth, $\theta_{step}$ = angular separation between two consecutive lamellae = (Final azimuth-Initial azimuth)/n

$zi = (Z + i * zstep)$ (3)

Z = Initial vertical distance, $z_{step}$ = (Final vertical distance-Initial vertical distance)/n

This results in a series of points with individual parameters, given by: [($r_1$, $\theta_1$, $z_1$), ($r_2$, $\theta_2$, $z_2$),….. ($r_i$, $\theta_i$, $z_i$),….. ($r_n$, $\theta_n$, $z_n$)].

The difference between the final and the initial azimuths of the points of the series, is expressed as the angle of rotation (S). As a series of points is equivalent to a layer/segment of the skeleton, the angle of rotation of the series also represents the angle of rotation of a layer/segment. This angle of rotation (S) of a series/layer, is given by:

295  $S = \theta step * n$ (4)

A set of spiral axes (i.e., a series of points), each with the same ~~numbers~~ number (n) of points, is needed to create the other layers/segments for the entire skeleton reconstruction. Two such consecutive series of points (in red and black colors respectively) are presented in Figs. 6b and 6c. The points (r, ө, z) of all consecutive series are defined following the Eqs. (1), (2), and (3). The initial radius (R) and the vertical distance (V) is the same for all the consecutive series of points. However,
300  the initial azimuth (Θ) is different for each of the series and depends on the angular separation between two consecutive series of points. If the angular separation between two consecutive series of points is given by p. Then, the value of ~~the~~ "p" can be calculated as:

$p = 360°/N$ (5)

where N is the total number of series (i.e., the total number of layers/segments) for the full skeletal reconstruction. As the
305  azimuth of the first point in the first series is $\theta_1$, therefore the azimuth of the first point of the second series will be ($\theta_1$+p). The $I^{th}$ series of points in N numbers of series (I<N) can be represented as:

Series-I: [(r$_1$, ($\theta_1$+(I-1)*p), z$_1$), (r$_2$, ($\theta_2$+(I-1)*p), z$_2$),….. (r$_i$, ($\theta_i$+(I-1)*p), z$_i$),….. (r$_n$, ($\theta_n$+(I-1)*p), z$_n$)].

### 4.3.3 Creation of a layer and a segment

The segmented lamella is assigned to each point in the series, creating the layer and segment composed of lamellae. The
310  inclination of the lamella is added by rotating it, as described in Figs. 5a and 5b. In the case of forming a layer (following model-1 of the microstructural arrangement), all the lamellae (n) are assigned a single value of angle of inclination ($\delta_A$ or $\delta_B$). This suggests that rotating all the lamellae of the series with an inclination of $\delta_A$ or $\delta_B$ formed layer-A or layer-B, respectively. For generating a segment (following model-2 of the microstructural arrangement), the lamellae are alternatingly assigned two distinct angles ($\delta_A$ and $\delta_B$) of inclination, indicating rotation of the alternative lamellae of the series with inclinations of $\delta_A$ and
315  $\delta_B$.

Considering that the first and the last points of the layer/segment represent the base and the apex of the skeleton, the tilt associated with the two points are $\tau_b$ and $\tau_a$, respectively. The tilt values consistently change from $\tau_b$ at the base to $\tau_a$ at the apex. Thus, the value of tilt for $i^{th}$ point (i<n) of the series (i.e., layer/segment) is given by the following equation:

$\tau i = \tau(i-1) + i * tilt - increment$ (6), tilt-increment = $(\tau_b$-$\tau_a)$/n.

320  The value of the tilt is given to each lamella in the layer/segment by rotating it as described in Figs. 5a and 5c.

The descriptions of all parameters lead to the next step of reconstructing the full skeleton. The two skeletal reconstruction models of the microstructural arrangement have been termed as the layer model and the segment model respectively. It is described earlier (in sections 2.2.1 and 2.2.2) that the total number (N) of layers/segments in the whole skeleton of *N. globulus* is calculated as 12. Thus, the angular separation between two consecutive layers/segments will, therefore, be p = 360°/12 =

325    30° (from Eq. (5)). However, the values of initial and final azimuths, initial radius and vertical distance, $r_{step}$, $z_{step}$, and the total number of lamellae (n) in a layer/segment are impossible to calculate without the segmentation of a layer/segment. As it is really difficult to separate one layer/segment of lamellae from the skeleton, we have applied several trials with different combinations of these values and have taken those values that give a space-filling layer/segment with the separated lamella. Importantly, the physical overlap between two consecutive lamellae is effectively close to zero. After the trials, the values of

330    different angles and lengths are taken such that the lamellae merely touch each other without any physical overlap. Therefore, a single voxel contains only one lamella. The results suggest that the total number of lamellae in one layer/segment (n) is 15. All the values of the parameters used to reconstruct the layers/segments, following different equations given in section 4.3.2, are given in Table 1.

Table 1: Values of the parameters for reconstructing layers/segments of ~~Nannoconus~~ *N. globulus*.

335

| Parameters | Values for layer model | Values for segment model |
|---|---|---|
| $\delta_A$ | 25° | 25° |
| $\delta_B$ | 40° | 40° |
| $\tau_a$ | -35° | -35° |
| Tilt-increment | 4.37° | 4.37° |
| $\tau_b$ | 30.38° | 30.38° |
| $\Theta$ | 0° | 0° |
| $\Theta_{step}$ | 36° | 6° |
| p | 30° | 30° |
| R | 0.005 μm | 0.005 μm |
| $r_{step}$ | 0.139 μm. | 0.139 μm. |
| Z | 0 μm | 0 μm |
| $z_{step}$ | 0.251 μm | 0.251 μm |
| n | 15 | 15 |
| N | 12 | 12 |

**4.3.4 Layer Model**

Values of each of the cylindrical coordinates ($r_i$, $\Theta_i$, $z_i$), inclinations ($\delta_A$ and $\delta_B$), and tilt ($\tau_i$) for individual lamella in the first layer (layer-A) are provided in Table 2. The relative changes of these values for each of the lamellae across the length (L) are

16

graphically represented in Fig. B4 in the Appendix. A total of 12 layers (six layer-A and six layer-B) are created, alternatively

340 putting I = 0 to I = 11 in series I and using the values of parameters (layer model) of Table 1. Two successive layers of -A and

-B and the full skeletal reconstruction are shown in Figs. 7a-7d.

**Table 2: Values of the radius, azimuth, vertical distance, inclination, and tilt of all the 15 lamellae of the first reconstructed layer-A of** ~~Nannoconus~~ *N. globulus***. The lamellae are labelled sequentially from A1 to A15.**

| Lamellae | Radius (r) (μm) | Azimuth (ө) (degree) | Vertical distance (z) (μm) | Inclination (δ) (degree) | Tilt (τ) (degree) |
|---|---|---|---|---|---|
| A1 | 2.09 | 0 | 0.47 | 20 | -35 |
| A2 | 2.23 | 36 | 0.72 | 20 | -30.33 |
| A3 | 2.37 | 72 | 0.98 | 20 | -25.66 |
| A4 | 2.51 | 108 | 1.23 | 20 | -20.99 |
| A5 | 2.65 | 144 | 1.48 | 20 | -16.32 |
| A6 | 2.79 | 180 | 1.73 | 20 | -11.65 |
| A7 | 2.93 | 216 | 1.98 | 20 | -6.98 |
| A8 | 3.07 | 252 | 2.23 | 20 | -2.31 |
| A9 | 3.21 | 288 | 2.48 | 20 | 2.36 |
| A10 | 3.35 | 324 | 2.73 | 20 | 7.03 |
| A11 | 3.49 | 360 | 2.98 | 20 | 11.7 |
| A12 | 3.35 | 396 | 3.23 | 20 | 16.37 |
| A13 | 3.21 | 432 | 3.49 | 20 | 21.04 |
| A14 | 3.07 | 468 | 3.74 | 20 | 25.71 |
| A15 | 2.93 | 504 | 3.99 | 20 | 30.38 |
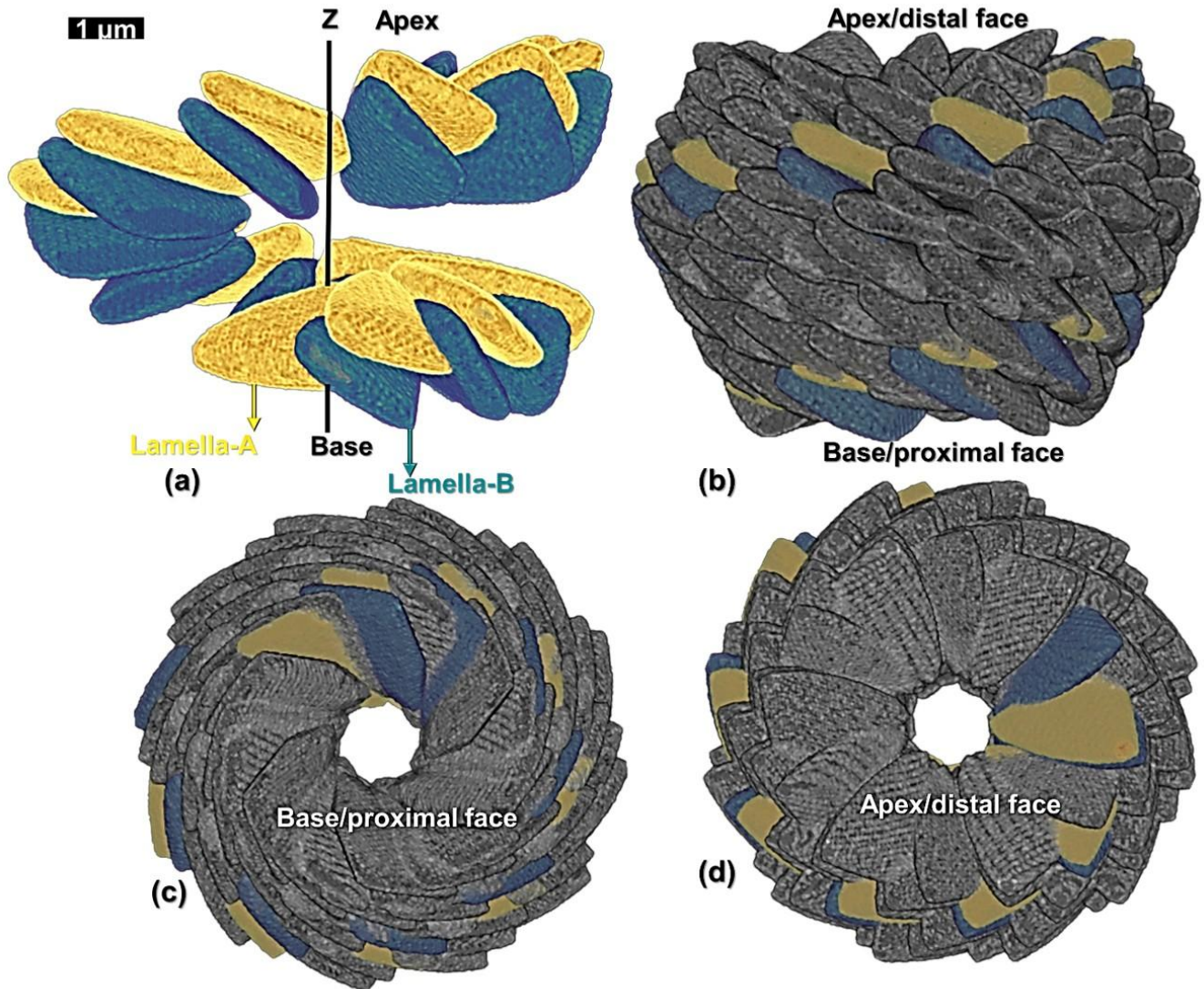
**Figure 7: Reconstruction of the skeleton of *N. globulus* using the layer model. (a) Longitudinal view of the two layers formed by lamella-A (yellow) and -B (green). (b, c, and d) Longitudinal, basal and apical views, respectively, of the combination of 12 such reconstructed layers forming the entire skeleton. The first two layers of lamellae-A and B are also shown. "Proximal" and "distal" (Aubry, 2013) terms refer to the orientation of the skeleton on the cell. Proximal face: face closest to the cell and distal face: face farthest from the cell.**

### 4.3.5 Segment Model

Values of each of the cylindrical coordinates ($r_i$, $\theta_i$, $z_i$), inclination ($\delta_A$ and $\delta_B$), and tilt ($\tau_i$) for individual lamella of the first reconstructed segment are given in Table 3. The graphical representation of their relative changes across the length (L) are presented in Fig. B5 in the Appendix. A total of 12 segments were generated using I = 0 to I = 11 in series I and the values of

355  parameters (segment model) of Table 1. A segment with the lamella -A and -B and the full skeletal reconstruction are shown in Figs. 8a-8d.

**Table 3: Values of the radius, azimuth, vertical distance, inclination, and tilt of all the 15 lamellae of the first reconstructed segment of ~~Nannoconus~~ N. globulus. The lamellae-A and -B are sequentially marked from A1 to A8 and B1 to B7, respectively.**

| Lamellae | Radius (r) (μm) | Azimuth (ɵ) (degree) | Vertical distance (z) (μm) | Inclination (δ) (degree) | Tilt (τ) (degree) |
|---|---|---|---|---|---|
| A1 | 2.09 | 0 | 0.47 | 20 | -35 |
| B1 | 2.23 | 36 | 0.72 | 20 | -30.33 |
| A2 | 2.37 | 72 | 0.98 | 20 | -25.66 |
| B2 | 2.51 | 108 | 1.23 | 20 | -20.99 |
| A3 | 2.65 | 144 | 1.48 | 20 | -16.32 |
| B3 | 2.79 | 180 | 1.73 | 20 | -11.65 |
| A4 | 2.93 | 216 | 1.98 | 20 | -6.98 |
| B4 | 3.07 | 252 | 2.23 | 20 | -2.31 |
| A5 | 3.21 | 288 | 2.48 | 20 | 2.36 |
| B5 | 3.35 | 324 | 2.73 | 20 | 7.03 |
| A6 | 3.49 | 360 | 2.98 | 20 | 11.7 |
| B6 | 3.35 | 396 | 3.23 | 20 | 16.37 |
| A7 | 3.21 | 432 | 3.49 | 20 | 21.04 |
| B7 | 3.07 | 468 | 3.74 | 20 | 25.71 |
| A8 | 2.93 | 504 | 3.99 | 20 | 30.38 |
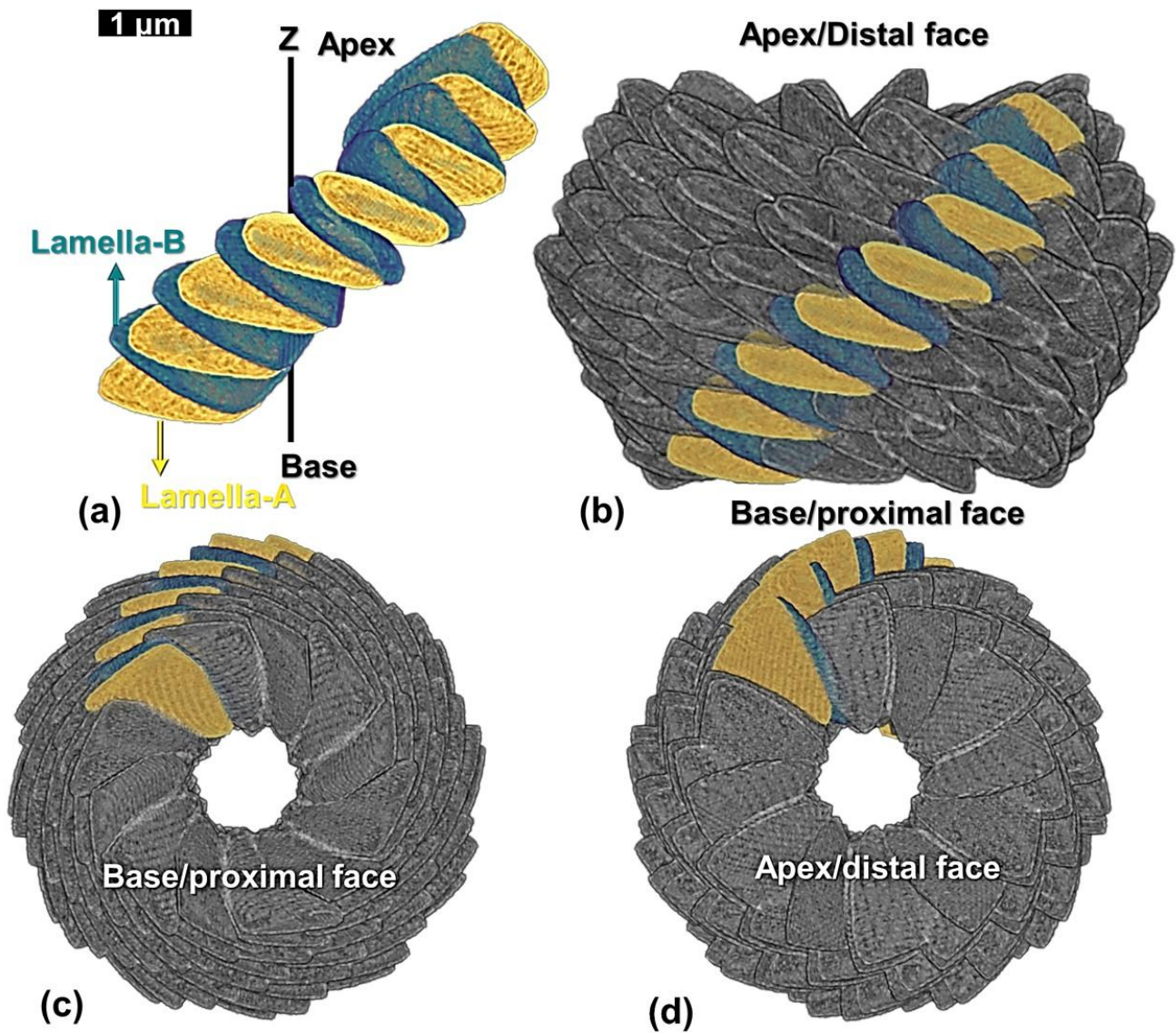
**Figure 8: Reconstruction of the skeleton of *N. globulus* using the segment model. (a) Longitudinal view with alternating, properly oriented, lamella-A (yellow) and -B (green). (b, c, and d) Longitudinal, basal and apical views, respectively, of the combination of 12 such reconstructed segments forming the entire skeleton. A segment containing alternatively placed lamella-A and -B is highlighted. "Proximal" and "distal" (Aubry, 2013) terms refer to the orientation of the skeleton on the cell. Proximal face: face closest to the cell and distal face: face farthest from the cell.**

## 5 Discussion

## 5.1 Which of the two models best explains the *Nannoconus* skeleton?

PXCT alone is insufficient to conclusively distinguish between the two models. However, it indeed provides the successful 3D reconstruction of the *Nannoconus* skeletal structure. The layer and segment models are based on two different concepts of skeletal microstructure of *N. globulus*. Both models result in similar reconstructions (Figs. 9a and 9b) of the skeleton, which structurally resembles the real specimen (Fig. 9c). Each of these two models of the microstructural arrangement suggests a distinct biomineralization process to form the entire skeleton. The first model implies that the skeleton is formed by lamellae organized in successive layers, whereas the second one involves that the skeleton is formed primarily of segments, each defined~~formed~~ by the stacking of lamellae. However, the following observations/arguments show that the layer model is insufficient to account for the structure of *Nannoconus*, and that the segment model is the right one. The layered structure of *Nannoconus* is distinctively visible in scanning electron microscope (SEM) images, but they are organized in segments, as it is clearly visible on one of the youngest species, *N. funiculus* (reported at ~90 Ma; Lees and Bown, 2016; Fig. B6a, in the appendix). ~~On the other hand,~~ Celear segment boundaries are observed in several species (Figs. B6a-d in the appendix), from the oldest one (*N. compressus*, reported at ~140 Ma; Bralower et al., 1989; Fig. B6d, in the appendix) to the youngest one (Fig. B6a, in the appendix). In many recrystallized or overgrown specimens, the individual layers are no longer visible; they have fused to form sorts of bricks, but the organisation in segments remains (Fig. B6d, in the appendix). As described ~~in~~ earlier, the Genus *Nannoconus* belongs to the Family *Nannoconaceae* (Reinhardt, 1966), which is included in the Order *Braarudosphaerales* (Aubry, 2013; Lees and Bown, 2016). This order also includes the Family *Braarudosphaeraceae*, which shares a strong evolutionary link with *Nannoconaceae*; and therefore, with *Nannoconus*, as described by Lees and Bown (2016) and Aubry (2025). According to Lees and Bown (2016), *Braarudosphaeraceae* are characterized by "five segments formed from stacks of non-imbricated laminae/elements", whereas *Nannoconaceae* are defined by "numerous stacked, imbricating elements." Here, "laminae/elements" refers to lamellae. *Braarudosphaera bigelowii* an extant species of *Braarudosphaeraceae*, with fossil representatives first occurring 100 Myr ago, calcifies a pentagonal skeleton with the combination of five trapezoidal segments (Fig. 4 in Hagino et al., 2016) composed of parallel "lamellae stacked in segments" (Aubry, 2013). Given the close evolutionary relationship between these two Families, it is reasonable to hypothesize that *Nannoconaceae* (and therefore, *Nannoconus*) may have calcified via a similar process, where imbricating lamellae were indeed stacked into segments.

1 μm

(a)                                                    (b)                                                    (c)
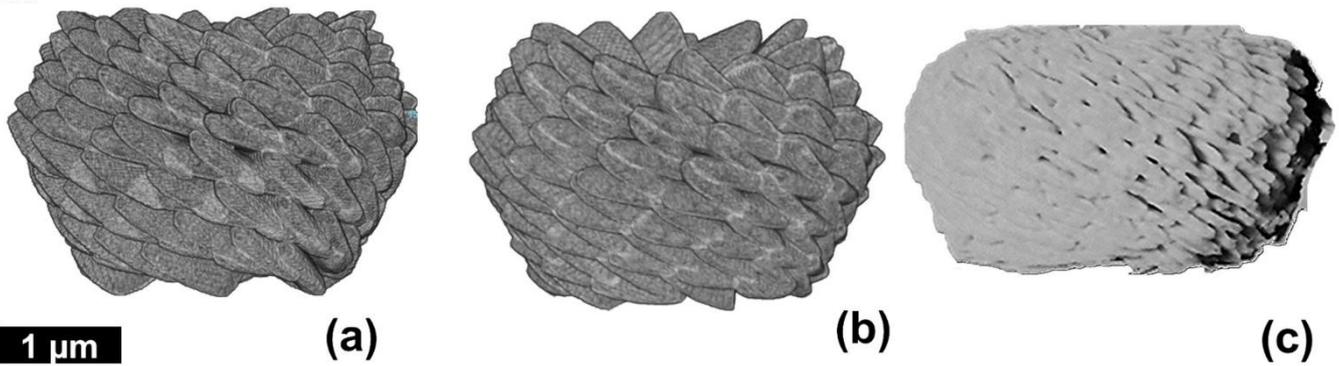
**Figure 9: Two different reconstructions of the entire skeleton of *N. globulus*. (a) reconstruction based on the layer model and (b) reconstruction based on the segment model. Similar skeletal reconstruction is also proposed by Aubry (2025); Fig. 12d. (c) External view of the specimen of *N. globulus* used in the PXCT experiment (see also Fig. 3b).**

## 5.2 Which parameters control *Nannoconus*'s skeletal morphology?

Considering the segment model, we now try to show which parameters control the inter-specific morphological variability observed within the *Nannoconus* group during the ~30 Myr of the Early Cretaceous. The parameters that can potentially control the morphology of the skeleton are the angle of rotation of the segment and the radius. The angle of rotation of each segment (Eq. (4) in section 4.3.2) is considered as 90° in the discussed reconstruction by the segment model. With the same ~~numbers~~ number of total segments (N = 12) and total lamellae in each segment (n = 15) used in the segment model, we have applied three different angles of rotations to individual segments: 30°, 60° and 180°. All of the angles of rotation used, resulted in reconstructed skeletons (Figs. 10a - 10d) of similar shape. So, it can be inferred that the angle of rotation of the segment does not affect the general shape of *Nannoconus*.



(a)                                    (b)                                    (c)                                    (d)
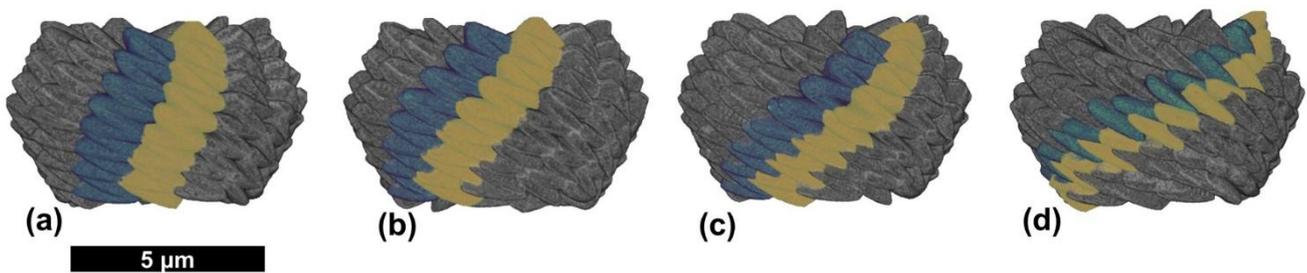
5 μm

**Figure 10: Four complete reconstructed *Nannoconus* skeletons based on the segment model with four different angles of rotation of each segment. (a-d) These angles of rotation are are 30°, 60°, 90°, and 180° respectively. Two consecutive segments of each reconstructed skeleton are marked in green and yellow.**

The other parameter that can potentially affect the morphology of the skeleton is the radius. As we discussed earlier, the particular way of changing the radius with the length (see Eq. (1)) resulted in the globular shape of the skeleton. Thus, different ways of changing the radius would give rise to different skeleton's morphologies. Five different morphologies (globular,

22

hour-glass, conical, barrel-shaped, cylindrical; Fig. 11) of the skeleton have been reconstructed by applying the same segment model using for each, the same values of the different parameters (Table 1) except for the radius (Table 4); they resemble the

415 morphologies of *Nannoconus* real species. Thus, it is determined that the radius is the parameter that controls the inter-specific morphological variability of *Nannoconus*. However, other than radius, the total number of the segments forming the entire skeleton could also vary for different species of *Nannoconus*. It should be kept in mind that in this discussion, the number of segments is considered to be 12 based on a SEM image of only one species, that is *N. globulus*. A comparative study of SEM images of different species of *Nannoconus* could be useful to investigate if the number of the segments in the skeleton is

420 ~~species dependent~~species-dependent. More generally, with the model of reconstruction described in this study, we have succeeded in creating a 3D skeleton of *Nannoconus*; that means that we could constrain changing skeleton's morphology not only at the level of the Genus, but also at the level of the Order of *Braarudosphaerales*, allowing us to investigate whether a particular skeleton morphology had been favoured during the long evolutionary history (~150 Ma) of this order. Recent research (Aubry, 2025) suggests that the importance of this Order lies in its distinct skeletal structure, indicating both a

425 taxonomic specificity and a unique biological position within the calcareous nannoplankton group.
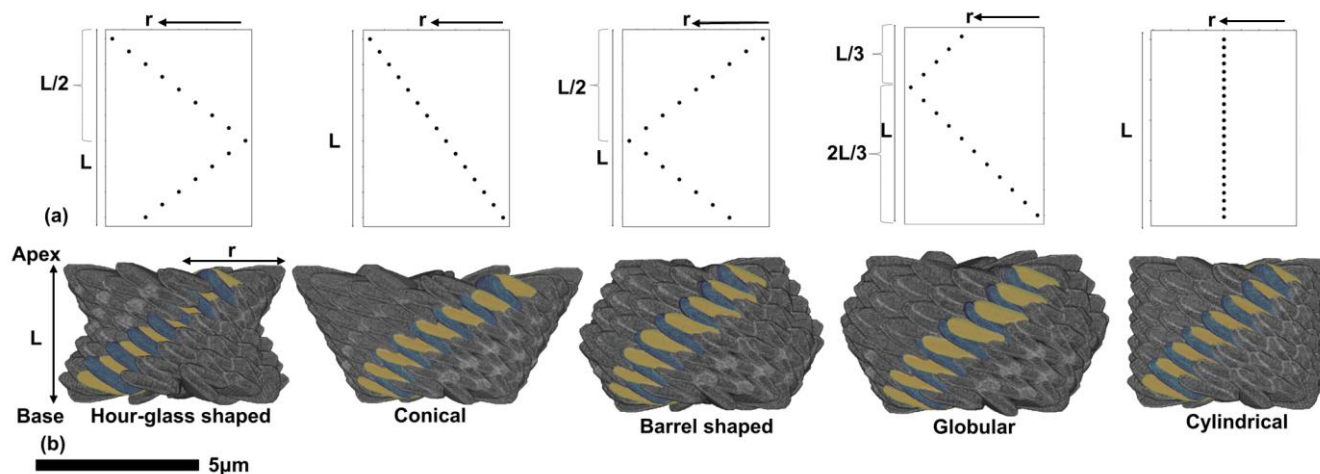


**Figure 11: Five different skeletal morphologies of *Nannoconus*, each with distinct variation of radius (r) across the length (L). (a) Graphical expressions of five different variations of radius along the length of the reconstructed skeleton, as shown in Table 4. Each of the points on the graphs indicate individual lamella of a segment. (b) Skeletons reconstructed following each of the possibilities,**
430 **using the segment model, with each skeleton highlighting a segment containing both types of lamellae-A (yellow) and -B (green).**

**Table 4: Five possible variations in radius along the length (from base to apex) of the reconstructed skeleton of *Nannoconus* are presented, each associated with distinct skeletal morphologies (as shown in Fig. 11). Corresponding species of *Nannoconus* exhibiting these respective morphologies are also provided.**

| Change of radius | Final morphology | Species |
|---|---|---|
| Radius decreases until ½ of the total length from the base and then increases to the apex | Hour-glass shaped | *N. abundans* |
| Radius constantly increases from the base to the apex | Conical | *N. steinmannii* |

23

| | | |
|---|---|---|
| Radius increases until ½ of the total length from the base and then decreases to the apex | Barrel shaped | *N. circularis* |
| Radius increases until 2/3$^{rd}$ of the total length from the base and then decreases to the apex | Globular | *N. globulus* |
| Radius is constant from the base to the apex | Cylindrical | *N. truittii* |

### 5.3 How were the segments of the *Nannoconus* skeleton biomineralized?

It is now important to infer the process of biomineralization of the segments of the *Nannoconus*. Inferences can be provided based on the comparison of the biomineralization process of *B. bigelowii*, as documented in Hagino et al., (2016). In an uncalcified living cell of *B. bigelowii*, an organic substrate is reported that resembles the shape of the pentagonal skeleton (Fig. B7a in the Appendix). The organic substrate is divided into five parts, with each of the parts mimicking the shape of a segment (Fig. B7b in the Appendix). In the vertical segments of the calcified skeleton produced by living *B. bigelowii*, thin organic layers are observed between two successive lamellae. Thus, the organic substrate and layers are seen to act as a "template" for the calcification of the segments and lamellae. This would indicate that the lamellae are stacked in each of the five parts of the organic substrate, templated by the organic layers, creating five segments. We suggest a similar process of calcification for *Nannoconus* with 12 segments; the calcification occurred on an organic "substrate" divided into 12 parts (since 12 segments are considered) (Fig. B7c in the Appendix). Additionally, lamellae in the segments of *Nannoconus* are placed with inclination and tilt, creating their interlocking arrangement, whereas they are parallel in the segments of *B. bigelowii*. The inclination and tilt are explained by two mutually perpendicular rotations of the lamellae (see section 4.3.1) of *Nannoconus*. Such rotations with specific directions (i.e., clockwise and anti-clockwise) are commonly observed in biomineralized skeletons produced by marine organisms; for example, the coiling of gastropod's shell (Ueshima and Asami, 2003), the overlapping of the chambers generated by foraminifera (Schiebel and Hemleben, 2017), microstructural imbrications of the calcite units in the skeletons produced by calcareous nannoplankton (Young et al., 1999; Aubry, 2013, 2025). It is implied that these rotations are influenced by biomolecules such as the proteins, amino acids, and polysaccharides (Young and Henriksen, 2003; Yu et al., 2005; Jiang et al., 2017, 2018, 2019). Was it the case for *Nannoconus*?

To discuss this point, we presented here the process of mineralization of vaterite (a polymorph of calcium carbonate, CaCO$_3$) induced by amino acid (Jiang et al., 2018). The growth occurs layer-by-layer with amino acid intervening between two consecutive layers to form the microstructure of the layered vaterite. The two layers are termed "mother" and "daughter" layers. The amino acid (i.e., Aspartic acid) present between the mother and the daughter layers, rotates the daughter layer clockwise (Figs. 6A and 6B in Jiang et al., 2018), creating a difference in inclination between the two layers. Thus, because of the presence of amino acid between the two consecutive layers, the "inclination" of the new layers added during growth, increases continuously. The amino acid induced rotation of the layered vaterite structurally resembles the interlocking

arrangement of the lamellae of *Nannoconus*. However, the reconstruction of the skeleton of *Nannoconus* showed that not only one but two rotations of the lamellae in two mutually perpendicular directions are necessary to develop the interlocking pattern (as discussed in section 4.3.1). Based on the comparison with the layer-by-layer grown vaterite, we hypothesize the probable presence of a layer of amino acid(s) or any biomolecule(s) to explain the two rotations between two successive lamellae of *Nannoconus*, creating the tilt and inclination. These successive lamellae could correspond respectively to the mother and daughter layers in the vaterite. For two such successive lamellae of a segment we call the preceding (similar to "mother layer" of Jiang et al., 2018) and succeeding (similar to "daughter layer" of Jiang et al., 2018) lamellae as the inferior and superior lamellae respectively (Fig. 12). The sense of the rotations to generate the inclination and tilt are marked in the inferior and superior lamellae in Fig. 12. The required arrangements for these two lamellae are: for inclination: opposite direction (both clock and anti-clockwise) of successive rotations (given by the black bold arrows in Fig. 12a), and, for tilt: the same direction (anti-clockwise) of successive rotations (given by the black dashed arrows in Fig. 12b). The opposite direction of rotations in the inferior and superior lamellae actually generate the two lamellar types i.e., lamella-A and -B. Therefore, both the clock and anti-clockwise rotations occur simultaneously during biomineralization of the superior lamella on the inferior lamella, generating the interlocking arrangement of the constituting lamellae. These possible explanations strengthen our initial hypothesis of the amino acid(s)/biomolecule(s) containing layer, between two successive lamellae. This layer, containing the amino acid(s)/biomolecule(s), could correspond to the organic substrate occurring as the "template" for the calcification of the segments of *Nannoconus*.

These organic layers, if they were present in the *Nannoconus* skeleton, are unlikely to be preserved in the fossil record. However, specimens of *Nannoconus* have been studied with confocal Raman micro-spectroscopy, and the obtained spectra have shown a signal that could be related to preserved organic matter the presence of preserved "organic matter signature" within the skeleton (Fig. B8 in the Appendix). The confocal Raman spectra of *Nannoconus* are characterized by a number of peaks, with distinct intensities at specific wavenumbers. The spectra present two distinct parts: one from 150 to 1200 cm$^{-1}$ with characteristic peaks of the skeletal $CaCO_3$, and the second one from 1200 to 2000 cm$^{-1}$, which could correspond to the "organic matter" signature preserved within the skeleton. Indeed, in a study focused on the identification of organic matter in bioclastic grains encountered in marine carbonate rocks, Moya et al., (2023) performed confocal Raman micro-spectroscopy and detected on the spectra the fingerprints of organic matter in the higher wavenumber region (i.e., wavenumber>1200 cm$^{-1}$). Additionally, Raman signals related to protein and polysaccharide are also reported in the same spectral region from biocalcite produced by extant calcareous nannoplankton (Silvestri et al., 2020). Therefore, a future investigation using tomographic technique with a resolution finer than the PXCT, such as atom probe tomography (resolution ~0.5 nm), could be useful to confirm the presence of organic matter preserved within the skeleton of *Nannoconus*.
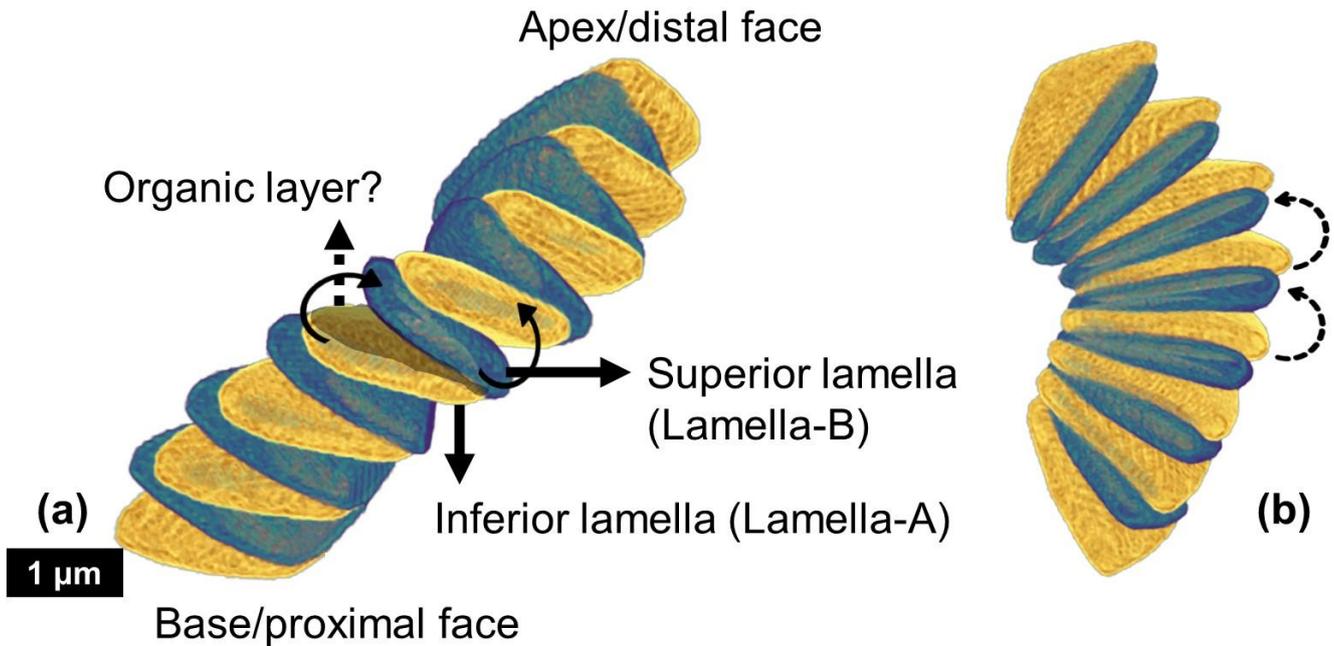
**Figure 12: Reconstructed segment of *N. globulus* with the proposed inferior and superior lamellae, along with the hypothesized intervening organic layer between them. (a) The two black bold arrows show the two opposite directions of rotation (clock and anti-clockwise), which create distinct inclinations in the two successive lamellae, generating the lamella-A (yellow) and -B (green). (b) Same segment, with two dashed black arrows presenting anti-clockwise rotations in two successive lamellae, generating the tilt in them.**

These organic layers, if they were present in the *Nannoconus* skeleton, are unlikely to be preserved in the fossil record. However, specimens of *Nannoconus* have been studied with confocal Raman micro-spectroscopy, and the obtained spectra have shown the presence of preserved "organic matter" within the skeleton (Fig. B8 in the Appendix). The confocal Raman spectra of *Nannoconus* are characterized by a number of peaks, with distinct intensities at specific wavenumbers. The spectra present two distinct parts: one from 150 to 1200 $cm^{-1}$ with characteristic peaks of the skeletal $CaCO_3$ and the second one from 1200 to 2000 $cm^{-1}$ which could correspond to the "organic matter" signature preserved within the skeleton. Indeed, in a study focused on the identification of organic matter in bioclastic grains encountered in marine carbonate rocks, Moya et al., (2023) performed confocal Raman micro-spectroscopy and detected on the spectra the fingerprints of organic matter in the higher wavenumber region (i.e., wavenumber>1200 $cm^{-1}$). Additionally, Raman signals related to protein and polysaccharide are also reported in the same spectral region from biocalcite produced by extant calcareous nannoplankton (Silvestri et al., 2020). Therefore, a future investigation using tomographic technique with resolution finer than the PXCT, such as atom probe tomography (resolution ~ 0.5 nm) could be useful to confirm the presence of organic matter preserved within the skeleton of *Nannoconus*.

The *Nannoconus* skeleton is reconstructed from a specimen of *N. globulus*. Although the specimen is generally well-preserved as seen in SEM images, PXCT observations at higher resolution reveal finer diagenetic alterations within the skeletal interior. Nevertheless, our reconstruction process enables the segmentation of individual lamellae and the generation of a 3D skeleton using geometric parameters, including tilt and inclination angles as well as radial length. To ensure accuracy, these geometric parameters i.e., radius, inclination, and tilt, were measured repeatedly, and the 3D skeleton was iterated through multiple trials to obtain the closest possible resemblance to the real skeleton. As a result, the internally detected diagenetic effects do not affect the validity of the 3D reconstruction allowing subsequent interpretations of biomineralization. The strategy is therefore independent of diagenetic alteration, and thus, applicable to explain the skeletal microstructure of *Nannoconus* specimens even with poor state of preservation. It is noteworthy that the 2D SEM images of various *Nannoconus* species from different geological settings and ages show that their skeletons consist of interlocking lamellae, and species differ in overall skeletal morphology. The PXCT-based 3D reconstruction of *N. globulus* as obtained from the segment model, clarifies this microstructure as: the interlocking pattern results from lamellae stacked at two distinct inclinations, and changes in radius control the general morphology. Thus, a single specimen provides sufficient geometric parameters to interpret 3D microstructure across species, and the resulting biomineralization inferences are applicable to *Nannoconus* species through different geological intervals. We have hypothesized above that the biomineralization of the lamellae of the *Nannoconus* segments is "templated" by an organic layer containing amino acid(s)/biomolecule(s). The rotations induced by the amino acid(s)/biomolecule(s) created the inclination and tilt associated with the lamellae, hence generating the interlocking arrangement of the lamellae. Both the clock and anti-clockwise rotations are inferred in the same skeleton of *Nannoconus*. Such "biomolecule(s)" influenced natural biomineralized 3D microstructure with repetitive arrangement of units like the calcite lamellae as observed in *Nannoconus*, are often studied to synthesize biomimetic materials (Jiang et al., 2019). These materials, engineered for enhanced physical (e.g., hardness) and chemical (e.g., solubility) properties (Cho et al., 2023), have applications in research fields like catalysis and biomedicine. Therefore, the 3D skeleton reconstruction of *Nannoconus* can definitely provide significant insights into biomimetic material design, expanding its relevance beyond Palaeontology.

## 6 Conclusion

Among calcareous nannofossils, the *Nannoconus* group of the Order *Braarudosphaerales* (fossil and extant representatives) presents sophisticated massive skeletons, organized in an interlocking arrangement of calcitic lamellae stacked in segments, forming a wall around a central canal. They contributed to huge carbonate accumulations over ~30 million years in the Early Cretaceous seas. The biomineralization process that led to the production of these massive skeletons was unknown. The aim of the present study was to obtain a proper understanding of this process from a 3D reconstruction of the skeleton. A set of Ptychography X-ray computed tomography (PXCT) with synchrotron radiation at the SWING Beamline of SOLEIL (French synchrotron) was applied on several well-preserved *Nannoconus* skeletons to understand the microstructural arrangement at

the nanometer level (finer than the thickness of a lamella). The result of the experiment was a series of tomographic image slices (3D resolution ~40 nm) for the skeleton. Then, one lamella, virtually separated from the image slices, is used to reconstruct the entire skeleton of *Nannoconus* in the ORS-Dragonfly software. For the first time, a 3D skeletal reconstruction has been achieved for *Nannoconus globulus*. The interlocking arrangement of the lamellae results from two different angles, termed inclination and tilt, while changing radius (minimum ~2.1 μm to maximum ~3.5 μm) controls the skeletal morphology. The 3D model of skeleton reconstruction developed in the present study could be further applied to the reconstruction of the skeleton of other Genera within the Order of *Braarudosphaerales* to investigate if a particular skeleton morphology has been favoured during the long evolutionary history of this order. The biomineralization of the segments is hypothesized to be templated by organic layers containing amino acid(s)/biomolecule(s). During the biomineralization of the lamellae, the amino acid(s)/biomolecule(s) is are proposed to have induced clockwise and anti-clockwise rotations, creating the inclination and tilt and therefore generating the interlocking arrangement of the lamellae. PXCT 3D reconstruction of the *Nannoconus* skeletal structure, combined with existing 2D SEM observation, as well as biomineralization hypotheses, supports the interpretation of the *Nannoconus* skeleton as being composed of "segments" in the same way as *Braarudosphaera* is and probably other Mesozoic nannofossils (Aubry 2025). Biomolecule(s)-driven naturally produced microstructures characterized by the repetition of units such as the 3D arrangement of the lamellae of *Nannoconus*'s skeleton, are often extensively investigated for designing biomimetic materials. Such materials with artificially enhanced physico-chemical properties (e.g., hardness, solubility) are implemented in research with specialisation to catalysis and biomedicine, therefore making this publication relevant and important, outside the study of calcareous nannofossils.
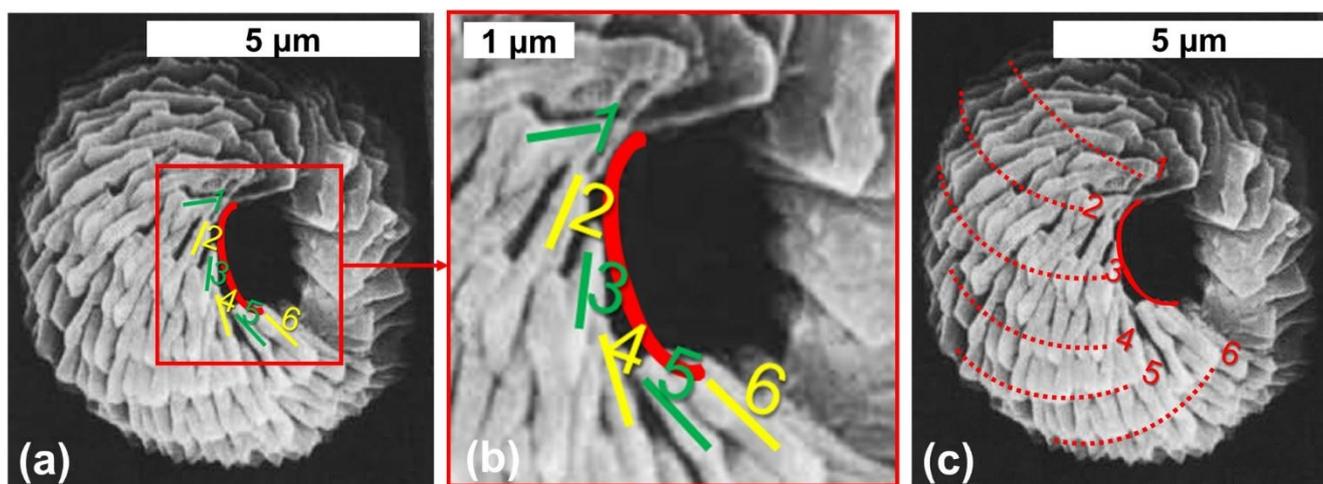
**Appendix A**



**Figure B1: Three-quarter view of the distal face of *N. globulus* in scanning electron microscopy (SEM). (a) Six lamellae in the 180° transect of the apex (given by the red curve) are highlighted. Three of lamellae-A and three of lamellae-B are numbered in green and yellow colours, respectively. (b) Magnified view of the part delineated by the red box in (a) with all the six lamellae: three**

28

lamellae-A (yellow) and three lamellae-B (green). (c) Boundaries between six segments highlighted by red-dotted lines in the same 180° transect of the apex of the *N. globulus*. SEM image modified from Covington and Wise, 1987.
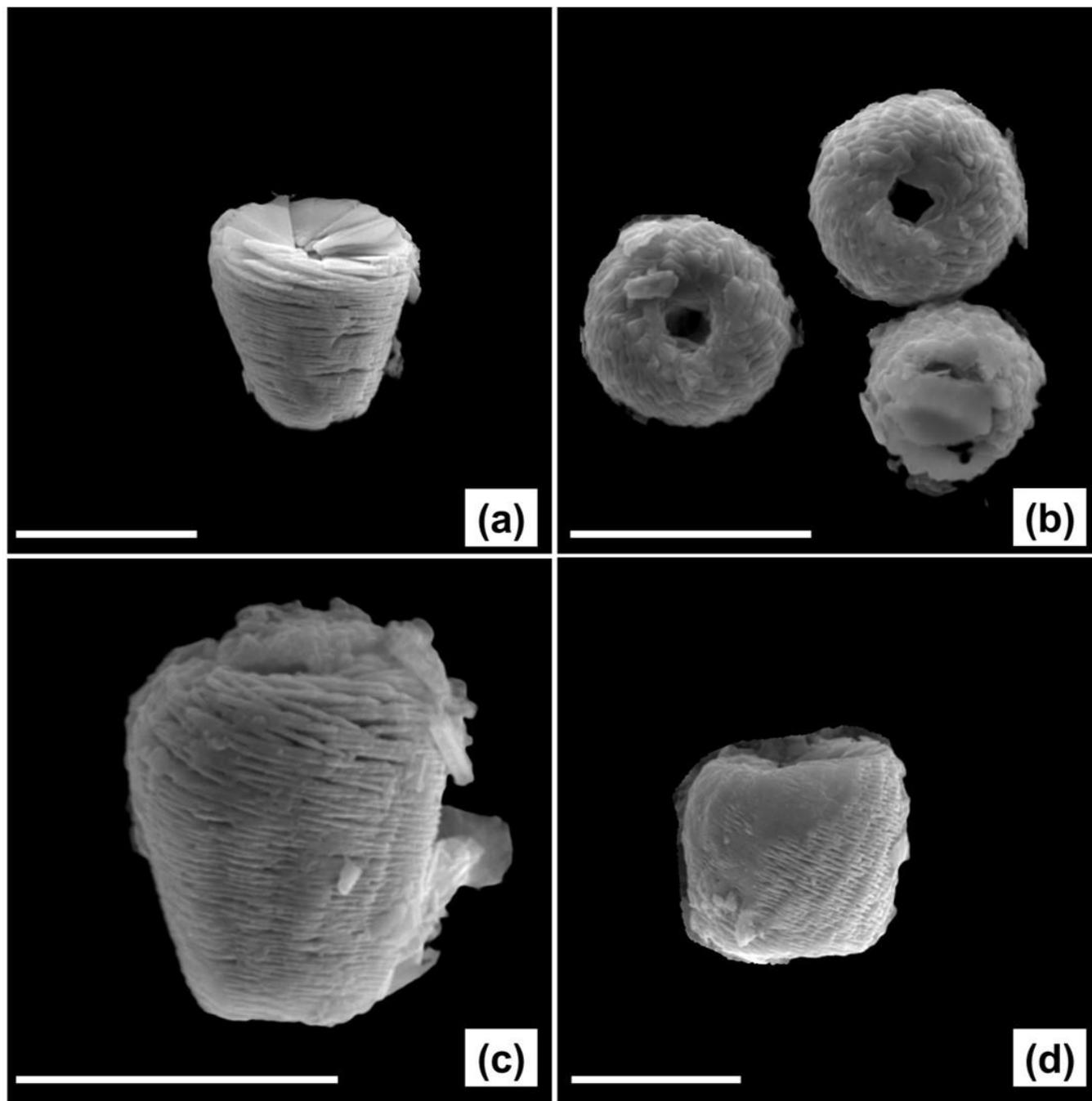


**Figure B2:** SEM images of well-preserved specimens of *Nannoconus*, from DSDP Leg-93-Site 603 (continental rise of the western margin of the North Atlantic) core 44, interval 115-116 cm. Individual lamella can be clearly distinguished in each of the specimens

thanks to their good preservation. Identification: (a) *N. steinmannii*, (b) *N. globulus*, (c) *N. kamptneri*, (d) *N. circularis*. The white line represents 10 μm.
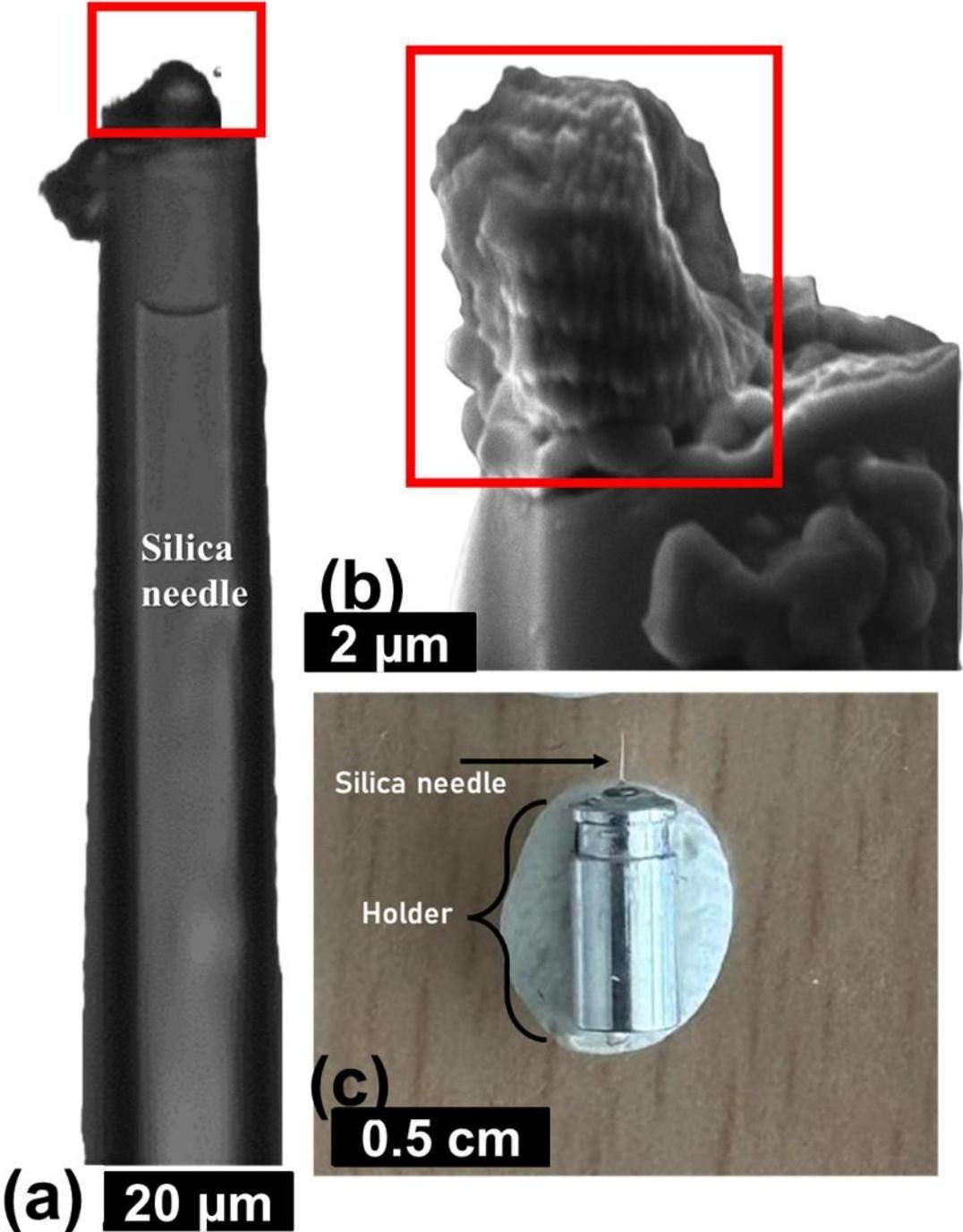
**Figure B3: Procedures used for the sample preparation of synchrotron-based ptychography X-ray computed tomography experiment, applied on *N. globulus*. (a)** A specimen of *N. globulus* (inside the red box) is manually picked with a silica needle. **(b)** SEM image of the specimen. **(c)** The needle with a *Nannoconus* resting at its tip is placed in a metal holder that fits in the experimental station of the beamline of the synchrotron radiation centre.
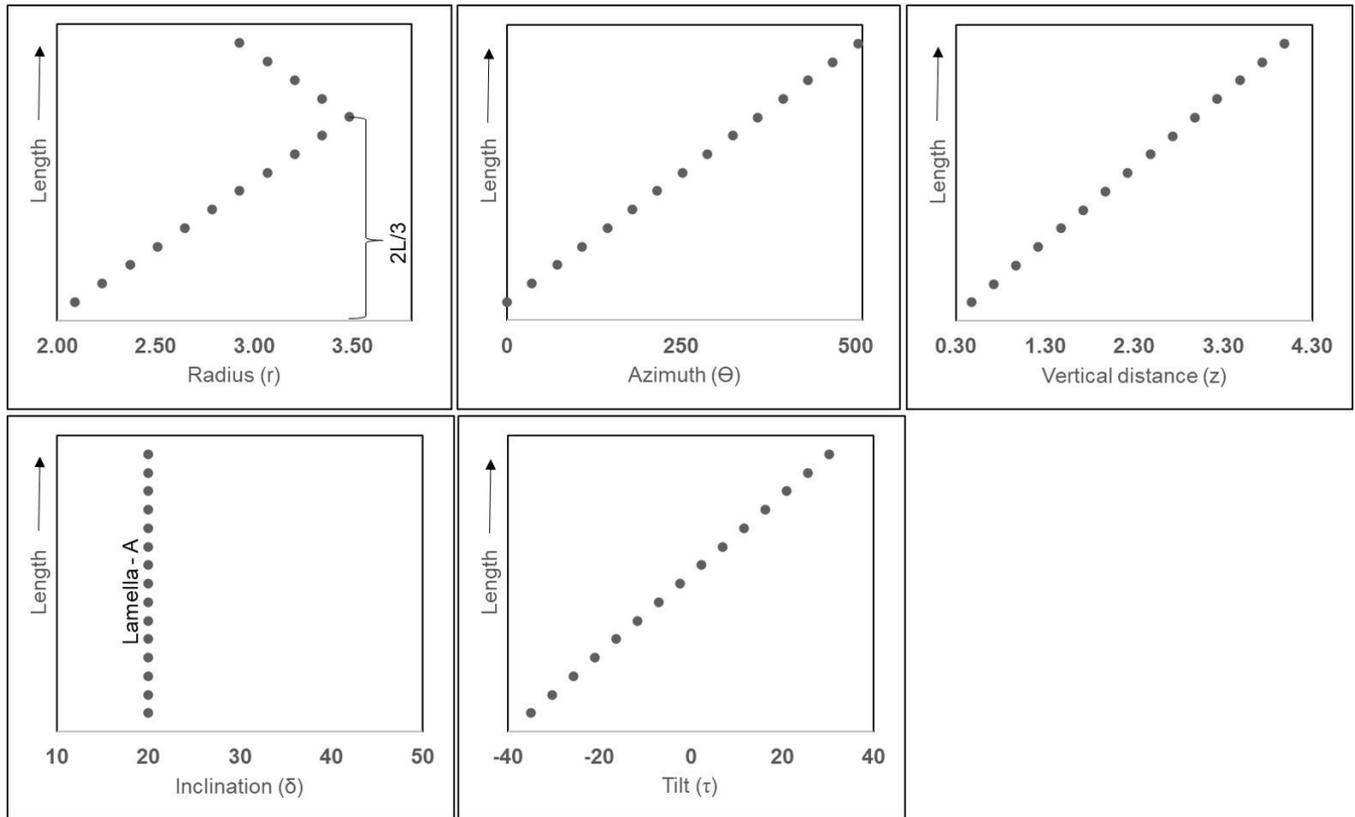


**Figure B4: Graphical representation showing the variation of parameters along the length (L) of the first reconstructed layer (layer-A) composed of lamella-A, of *N. globulus*. The black points in the graphs, mark individual lamellae.**
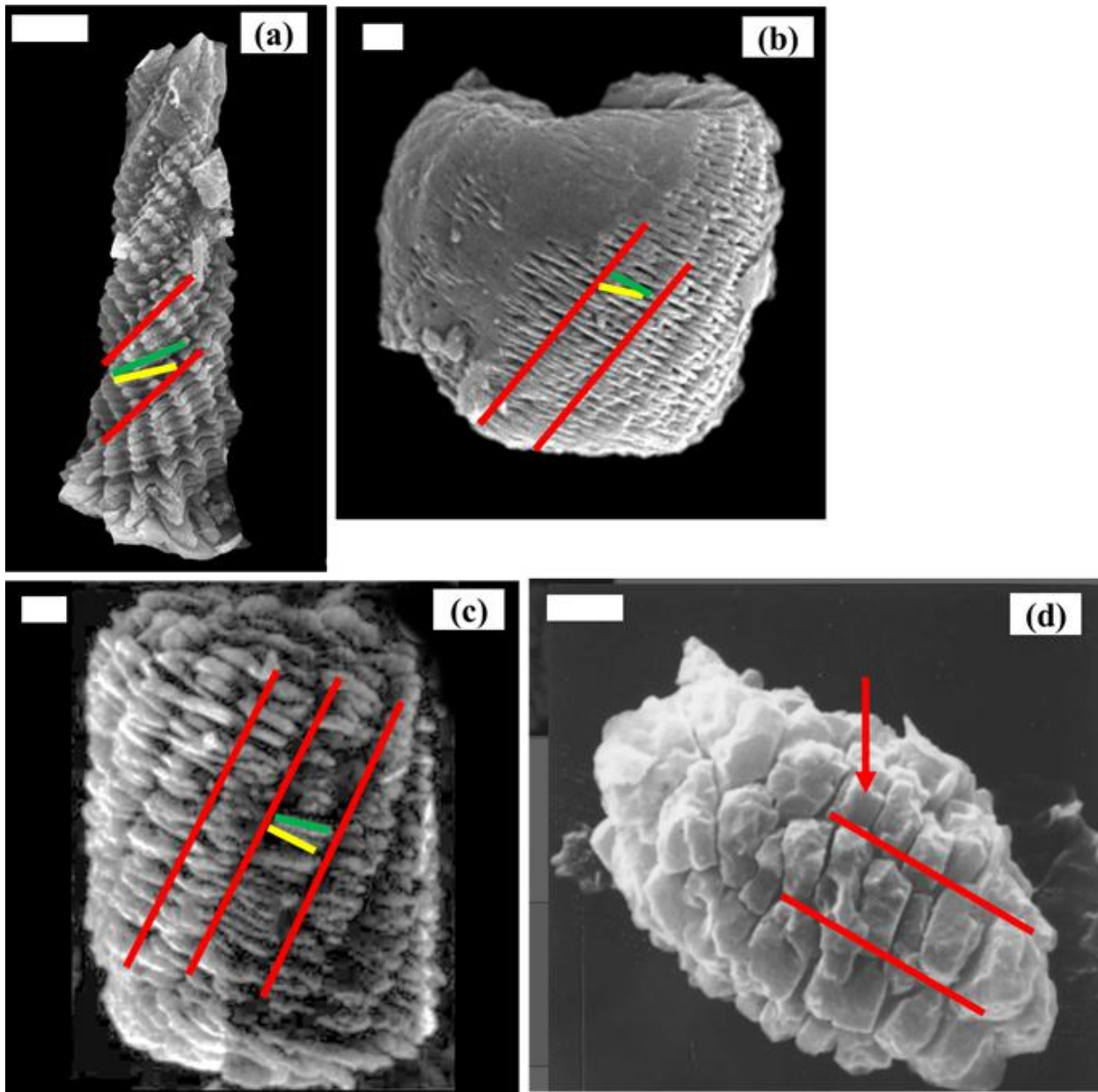
31
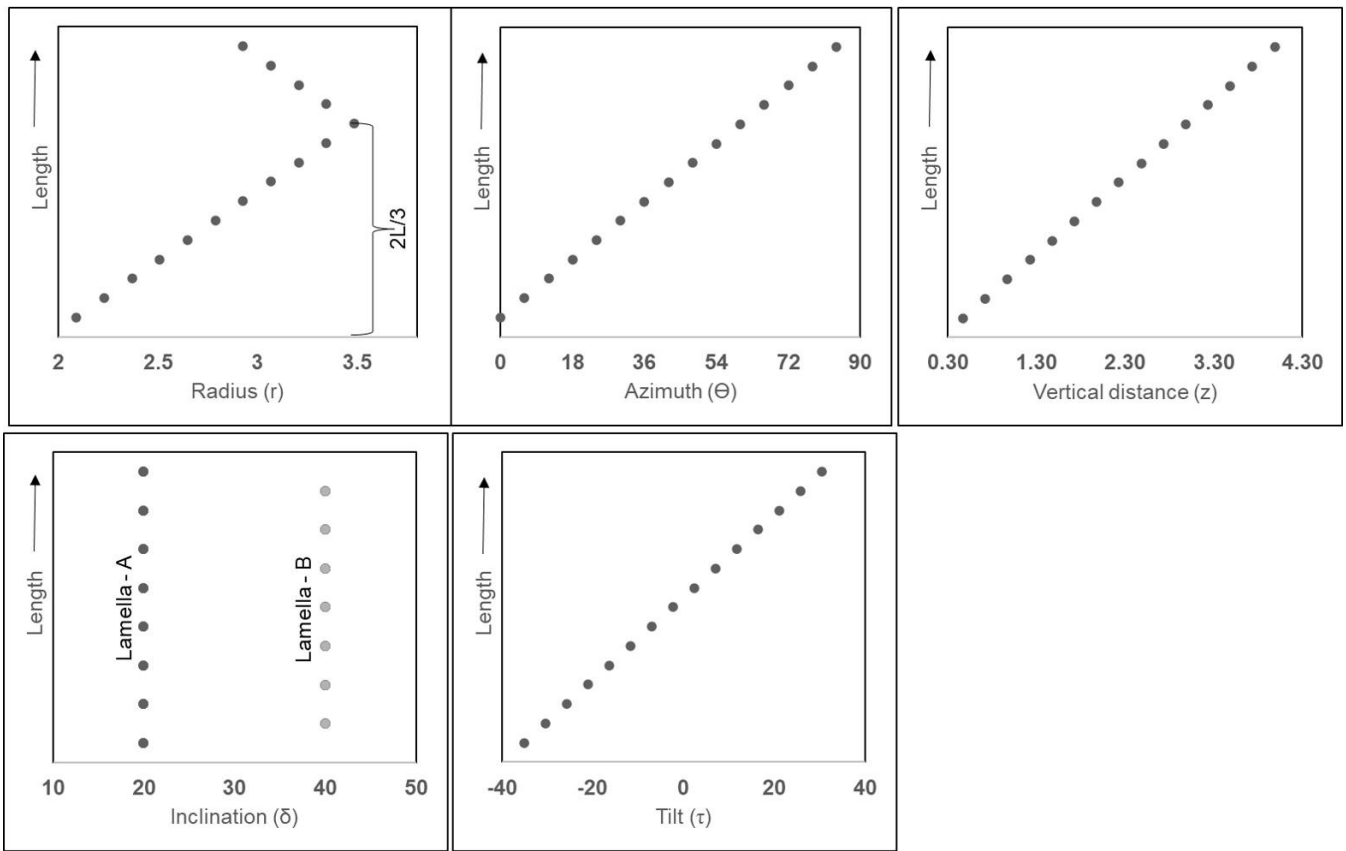
**Figure B5: Graphical representation showing the variation of parameters along the length (L) of the first reconstructed segments composed of lamella-A and -B of *N. globulus*. The black points in the graphs, mark individual lamellae.**

585 **Figure B6: SEM images of different species of *Nannoconus*, with the segments, marked in red lines along with lamella-A (yellow line) and -B (green line). (a) *N. funiculus*; adapted from Lees and Bown (2016). (b) *N. globulus*, from DSDP Leg-93-Site 603 (continental rise of the western margin of the North Atlantic; core 44, interval 115-116 cm) presented in Fig. B2d in this study. (c) *N. truittii*; adapted from Hattner and Wise (1980), as available in the Nannotax3 website (Young et al., 2022). (d) *N. compressus*; adapted from Bown and Cooper (1998). The red arrows indicate lamellae that have fused and thickened due to overgrowth. The two**
590 **types of lamellae (i.e., -A and -B) cannot be distinguished separately. This specimen, however, has preserved the organization of the segments. The white bar represents 1 μm.**
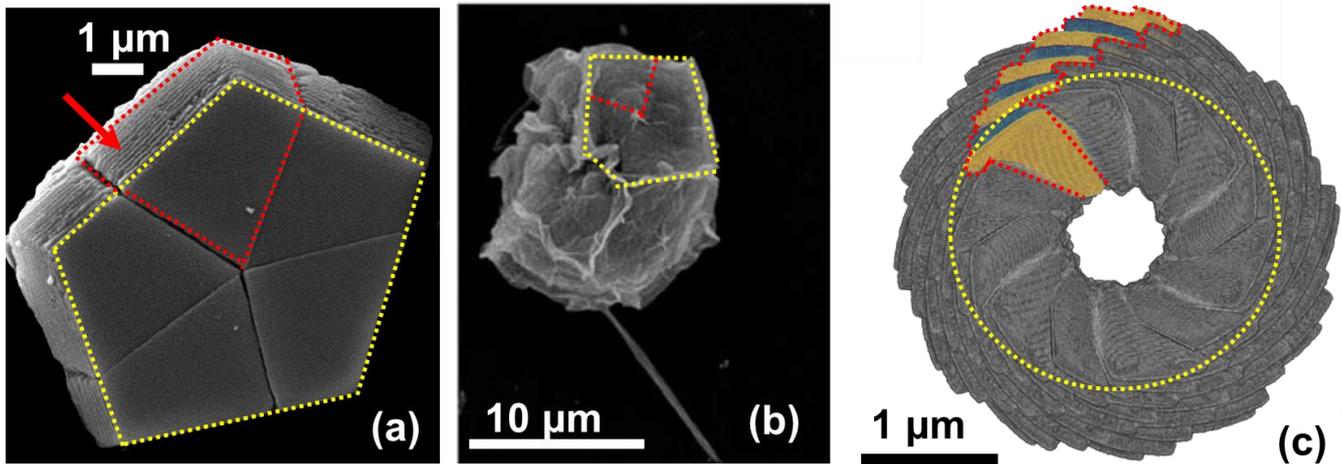
**Figure B7: Comparison between the *B. bigelowii* and the reconstructed *N. globulus*. (a)** SEM image of the pentagonal skeleton of *B. bigelowii*, adapted from Bown, 2010. The yellow dotted lines mark the boundaries of the pentagonal skeleton and the red dotted lines represent a segment. The red arrow indicates the parallel stacking of the lamellae, forming a segment. **(b)** The organic substrate, acts as template for the calcification of *B. bigelowii*. The yellow dotted lines represent the boundary of the substrate that resembles the pentagonal skeleton. The substrate is divided into five parts, with one part marked by the red dotted lines, mimicking the shape of the segment. Image adapted from Hagino et al., 2016. **(c)** The basal view of the reconstructed skeleton of *N. globulus*. The yellow dotted circle represents the "probable" organic substrate, acting as template for the calcification of *Nannoconus*. The substrate is divided into 12 parts (as *Nannoconus* is considered to have 12 segments), with the boundaries of one part marked by the red dotted lines.
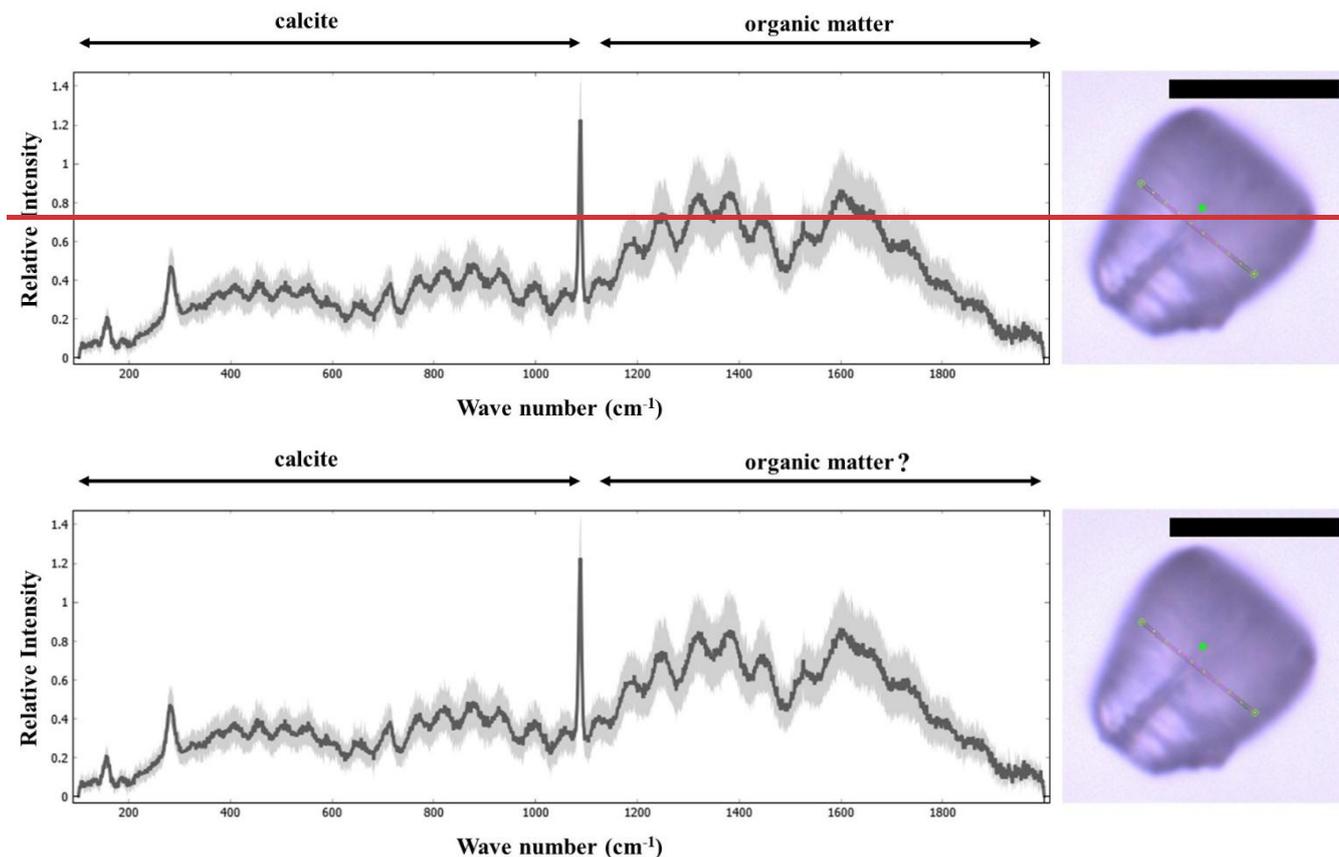
Figure B8: Confocal Raman spectra of *Nannoconus* displaying two regions corresponding to the compositional CaCO₃ and the "organic matter" preserved within the skeleton. The photomicrograph in optical microscopy (PPL) of the *Nannoconus* is given on the right, with a red line showing the scanning path for the spectra. The black scale bar represents 10 μm. PPL: plane-polarized light. The Raman spectra were obtained using a LabRAM Soleil Horiba Raman micro spectrometer with 532 nm wavelength laser-excitation and 1 μm spot size. A laser power of 1.1 mW was used to confirm that there is no damage tof the specimens induced by the laser. The laser beam was focused on the sample through a hole of 50 μm using an objective at 100X magnification. The specimen was subjected to linear scans along the surface (5-10 μm) and also inside the specimen (4-5 μm). A total 25 scans were recorded, each with an acquisition time of 2 seconds. Peaks were fitted in the spectrum using Gaussian functions in Quasar software (Toplak et al., 2017) as a part of the analyses. The spectra have been normalized to the maximum intensity. The black spectrum represents the average of all 25 recorded spectra of the *Nannoconus*.

**Code availability**

The code for the skeletal reconstruction of *Nannoconus globulus* for both the layer and segment models is available in the repository: https://doi.org/10.5281/zenodo.14925063 (Chowdhury et al., 2025).

The segmentation, reconstruction, and visualization of the results have been done in Dragonfly software version 2024.2 for [windows]. Comet Technologies Canada Inc., Montreal, Canada; software available at https://www.theobjects.com/dragonfly.

## Sample availability

Rock samples and associated nannofossil samples used for the experiment are curated at the Collections de Géologie de l'Observatoire des Sciences de l'Univers de Grenoble (OSUG), with an appropriate UJF-ID number. OSUG-COLLECTIONS is a database of rocks, minerals, and fossils, https://web.collections.osug.fr, OSUG, UGA. doi:10.17178/OSUG-COLLECTIONS.all.

## Author contributions

RC prepared the sample with inputs from **BSM**, **FG**, **AK,** and **AFM**, applied the image segmentation, co-developed the reconstruction code with **AFM,** and wrote the original draft. **JCS**, **JLH,** and **AK** helped in the initial conceptualization of the experiment. **MPA** intensely contributed to the conceptualization of the segment model of the reconstruction. **RC**, **RB**, **BSM**, **MD**, **AK**, **JP**, **FG,** and **AFM** performed the experiments in the synchrotron radiation centre. **FG** and **AFM** jointly supervised **RC** in this work and acquired all the relevant funding. All the co-authors contributed significant inputs for the review and editing.

## Competing interests

The authors declare that they have no conflict of interest.

## References

Aubry, M.P.: Remarques sur la systématique des Nannoconus de la craie., 1974.

Aubry, M.P.: Cenozoic Coccolithophores: Braarudosphaerales, Atlas of Micropaleontology series Micropaleontology Press, New York (336 pp), 2013.

Aubry, M.P.: Biomineralization in the Calcareous Nannoplankton Phenotypic Expressions Across Life Cycles, Geometric Control on Diversification, and Origin, Minerals, 15, 322, 2025.

Beuvier, T., Probert, I., Beaufort, L., Suchéras-Marx, B., Chushkin, Y., Zontone, F., and Gibaud, A.: X-ray nanotomography of coccolithophores reveals that coccolith mass and segment number correlate with grid size, Nature communications, 10, 751, 2019.

Bouché, P.: Eléments pour une définition d'un stratotype du Barrémien. Etat des connaissances sur les Nannofossiles calcaires du Crétacé inférieur, Mémoires du Bureau de Recherches Géologiques et Minières, 34, 451–459, 1965.

Bown, P. and Cooper, M.: Jurassic, Calcareous nannofossil biostratigraphy, 34–85, 1998.

Bown, P. R.: Cenozoic calcareous nannofossil biostratigraphy, ODP Leg 198 Site 1208 (Shatsky Rise, northwest Pacific Ocean), in: Proceedings of the Ocean Drilling Program, scientific results, 1–44, 2005.

Bown, P. R.: Calcareous nannofossils from the Paleocene/Eocene Thermal Maximum interval of southern Tanzania (TDP Site 14)., Journal of Nannoplankton Research, 31, 11–38, 2010.

Bralower, T. J., Monechi, S., and Thierstein, H. R.: Calcareous nannofossil zonation of the Jurassic-Cretaceous boundary interval and correlation with the geomagnetic polarity timescale, Marine Micropaleontology, 14, 153–235, 1989.

Bronnimann, P.: Microfossils incertae sedis from the Upper Jurassic and Lower Cretaceous of Cuba, Micropaleontology, 28–51, 1955.

Cho, N. H., Guerrero-Martínez, A., Ma, J., Bals, S., Kotov, N. A., Liz-Marzán, L. M., and Nam, K. T.: Bioinspired chiral inorganic nanomaterials, Nature Reviews Bioengineering, 1, 88–106, 2023.

Chowdhury, R., Fernandez-Martinez, A., and Giraud, F.: Code for the 3D submicron-scale skeletal reconstruction of Nannoconus, Zenodo, https://doi.org/10.5281/zenodo.14925063, 2025.

Covington, J.M., and Wise, S.W.: Calcareous nannofossil biostratigraphy of a lower Cretaceous Deep-sea fan complex: Deep-Sea Drilling Project Leg-93 Site-603, Lower Continental Rise. Initial Reports of the Deep Sea Drilling Project, 93, 617-660, 1987.

Derès, F. and Achériteguy, J.: Contribution à l'étude des Nannoconidés dans le Crétacé inférieur du Bassin d'Aquitaine, Mémoires du Bureau de Recherches Géologiques et Minières, 77, 153–159, 1972.

Derès, F. and Achériteguy, J.: Biostratigraphie des Nannoconides. Bulletin des Centres de Recherches Exploration-Production Elf-Aquitaine, 4, 1-53, 1980.

Dierolf, M., Menzel, A., Thibault, P., Schneider, P., Kewish, C. M., Wepf, R., Bunk, O., and Pfeiffer, F.: Ptychographic X-ray computed tomography at the nanoscale, Nature, 467, 436–439, https://doi.org/10.1038/nature09419, 2010.

Erba, E.: Nannofossils and superplumes: The Early Aptian "nannoconid crisis," Paleoceanography, 9, 483–501, https://doi.org/10.1029/94PA00258, 1994.

Erba, E.: The first 150 million years history of calcareous nannoplankton: Biosphere–geosphere interactions, Palaeogeography, Palaeoclimatology, Palaeoecology, 232, 237–250, https://doi.org/10.1016/j.palaeo.2005.09.013, 2006.

Farinacci, A.: Microorganismi dei calcari „Maiolica" e „Scaglia" osservati al microscopio elettronico (Nannoconi e coccolithophoridi), Bollettino della Società Paleontologica Italiana, 3, 172–181, 1964.

Hagino, K., Tomioka, N., Young, J. R., Takano, Y., Onuma, R., and Horiguchi, T.: Extracellular calcification of Braarudosphaera bigelowii deduced from electron microscopic observations of cell surface structure and elemental composition of pentaliths, Marine Micropaleontology, 125, 85–94, https://doi.org/10.1016/j.marmicro.2016.04.002, 2016.

Hart, M., Hylton, M., Oxford, M., Price, G., Hudson, W., and Smart, C.: The search for the origin of the planktic Foraminifera, Journal of the Geological Society, 160, 341–343, 2003.

Hattner, J. G., and Wise, S. W.: Upper Cretaceous calcareous nannofossil biostratigraphy of South Carolina. South Carolina Geology, 24, 41-117 1980.

Henriksen, K., Young, J. R., Brown, P. R., and Stipp, S. L. S.: Coccolith biomineralisation studied with atomic force microscopy, Palaeontology, 47, 725–743, https://doi.org/10.1111/j.0031-0239.2004.00385.x, 2004.

Hoffmann, R., Kirchlechner, C., Langer, G., Wochnik, A. S., Griesshaber, E., Schmahl, W. W., and Scheu, C.: Insight into Emiliania huxleyi coccospheres by focused ion beam sectioning, Biogeosciences, 12, 825–834, https://doi.org/10.5194/bg-12-825-2015, 2015.

Jiang, W., Pacella, M. S., Athanasiadou, D., Nelea, V., Vali, H., Hazen, R. M., Gray, J. J., and McKee, M. D.: Chiral acidic amino acids induce chiral hierarchical structure in calcium carbonate, Nature communications, 8, 15066, 2017.

Jiang, W., Pacella, M. S., Vali, H., Gray, J. J., and McKee, M. D.: Chiral switching in biomineral suprastructures induced by homochiral L-amino acid, Science advances, 4, eaas9819, 2018.

695  Jiang, W., Yi, X., and McKee, M. D.: Chiral biomineralized structures and their biomimetic synthesis, Materials Horizons, 6, 1974–1990, 2019.

Kamptner, E.: Nannoconus steinmanni nov. gen., nov. spec., ein merkwürdiges gesteinsbildendes Mikrofossil aus dem jüngeren Mesozoikum der Alpen, Paläontologische Zeitschrift, 13, 288–298, 1931.

Kooistra, W. H., Gersonde, R., Medlin, L. K., and Mann, D. G.: The origin and evolution of the diatoms: their adaptation to a
700  planktonic existence, Evolution of primary producers in the sea, 207–249, 2007.

Ky, F.: Convex sets and their applications, Argonne National Laboratory, 1959.

Lees, J. A. and Bown, P. R.: New and intriguing calcareous nannofossils from the Turonian (Upper Cretaceous) of Tanzania, Journal of Nannoplankton Research, 36, 83–95, 2016.

Moya, A., Giraud, F., Molinier, V., Perrette, Y., Charlet, L., Van Driessche, A., and Fernandez-Martinez, A.: Exploring
705  carbonate rock wettability across scales: Role of (bio)minerals, Journal of Colloid and Interface Science, 642, 747–756, https://doi.org/10.1016/j.jcis.2023.03.197, 2023.

Perch-Nielsen, K. 1985.: Mesozoic calcareous nannofossils, in: Bolli H.M., Saunders J.B., and Perch-Nielsen K. (Eds).: Plankton Stratigraphy, Cambridge University Press, Cambridge: 329–426, 1985.

Reinhardt, P.: Zur Taxionomie und Biostratigraphie des fossilen Nannoplanktons aus dem Malm, der Kreide und dem Alttertiär
710  Mitteleuropas: mit 1 Tabelle, PhD Thesis, Dt. Verlag für Grundstoffindustrie, 1966.

Reza, A. M.: Realization of the contrast limited adaptive histogram equalization (CLAHE) for real-time image enhancement, Journal of VLSI signal processing systems for signal, image and video technology, 38, 35–44, 2004.

Reznikov, N., Buss, D. J., Provencher, B., McKee, M. D., and Piché, N.: Deep learning for 3D imaging and image analysis in biomineralization research, Journal of Structural Biology, 212, 107598, 2020.

715  Schiebel, R. and Hemleben, C.: Planktic foraminifera in the modern ocean, Springer, 2017.

Siesser, W. G. and Winter, A.: Coccolithophores, Cambridge University Press, 1994.

Silvestri, A., Pätzold, J., Fratzl, P., Scheffel, A., and Faivre, D.: Surface-Enhanced Raman Scattering Microspectroscopy Enables the Direct Characterization of Biomineral-Associated Organic Material on Single Calcareous Microskeletons, J. Phys. Chem. Lett., 11, 8623–8629, https://doi.org/10.1021/acs.jpclett.0c02041, 2020.

720 Stradner, H. and Grün, W.: On Nannoconus abundans nov. spec. and on laminated calcite growth in Lower Cretaceous nannofossils, Verhandlungen der Geologischen Bundesanstalt, 2, 267–283, 1973.

Suchéras-Marx, B., Giraud, F., Simionovici, A., Daniel, I., and Tucoulou, R.: Perspectives on heterococcolith geochemical proxies based on high-resolution X-ray fluorescence mapping, Geobiology, 14, 390–403, https://doi.org/10.1111/gbi.12177, 2016a.

725 Suchéras-Marx, B., Giraud, F., Lena, A., and Simionovici, A.: Picking nannofossils: How and why, Journal of Micropalaeontology, 36, 219–221, https://doi.org/10.1144/10.1144jmpaleo2016-013, 2016b.

Suchéras-Marx, B., Mattioli, E., Allemand, P., Giraud, F., Pittet, B., Plancq, J., and Escarguel, G.: The colonization of the oceans by calcifying pelagic algae, Biogeosciences, 16, 2501–2510, https://doi.org/10.5194/bg-16-2501-2019, 2019.

Toplak, M., Birarda, G., Read, S., Sandt, C., Rosendahl, S., Vaccari, L., Demšar, J., and Borondics, F.: Infrared orange:
730 connecting hyperspectral data with machine learning, Synchrotron Radiation News, 30, 40–45, 2017.

Trejo, H.: La familia Nannoconidae y su alcance estratigrafico en America: Boletin de la Asociacion Mexicana de Geologos Petroleros, v. 12, 1960.

Ueshima, R. and Asami, T.: Single-gene speciation by left–right reversal, Nature, 425, 679–679, 2003.

Van Niel, B.: A review of the terminology used to describe the genus Nannoconus (calcareous nannofossil, incertae sedis),
735 Cahiers de Micropaléontologie, 9, 29–55, 1994.

Van Niel, B. E.: Early CretaceousNannoconus'(calcareous nannofossil, incertae sedis) in NW Europe, University of London, University College London (United Kingdom), 1993.

Van Rossum, G. and Drake, F. L.: Python 3 Reference Manual, CreateSpace, Scotts Valley, CA, 2009.

Wakonig, K., Stadler, H.-C., Odstrčil, M., Tsai, E. H., Diaz, A., Holler, M., Usov, I., Raabe, J., Menzel, A., and Guizar-
740 Sicairos, M.: PtychoShelves, a versatile high-level framework for high-performance analysis of ptychographic data, Journal of applied crystallography, 53, 574–586, 2020.

Walker, J., Marzec, B., Ozaki, N., Clare, D., and Nudelman, F.: Morphological development of Pleurochrysis carterae coccoliths examined by cryo-electron tomography, Journal of Structural Biology, 210, 107476, 2020.

745 Walker, J. M., Greene, H. J. M., Moazzam, Y., Quinn, P. D., Parker, J. E., and Langer, G.: An uneven distribution of strontium in the coccolithophore Scyphosphaera apsteinii revealed by nanoscale X-ray fluorescence tomography, Environmental Science: Processes and Impacts, 26, 966–974, https://doi.org/10.1039/d3em00509g, 2024.

Young, J. R. and Henriksen, K.: Biomineralization within vesicles: the calcite of coccoliths, Reviews in mineralogy and geochemistry, 54, 189–215, 2003.

Young, J. R., Davis, S. A., Bown, P. R., and Mann, S.: Coccolith Ultrastructure and Biomineralisation, 1999.

750 Young, J.R., Bown P.R., and Lees J.A.: Nannotax3 website, International Nannoplankton Association, Accessed 29 September 2025, www.mikrotax.org/Nannotax3, 2022.

Yu, S.-H., Cölfen, H., Tauer, K., and Antonietti, M.: Tectonic arrangement of BaCO3 nanocrystals into helices induced by a racemic block copolymer, Nature Materials, 4, 51–55, 2005.